Monthly Notices of the ROYAL ASTRONOMICAL SOCIETY

MNRAS **530,** 4501–4518 (2024) https://doi.org/10.1093/mnras/stae1121
Advance Access publication 2024 April 25

Discovery and follow-up of ASASSN-23bd (AT 2023clx): the lowest redshift and luminosity optically selected tidal disruption event

W. B. Hoogendam [1★] J. T. Hinkle [1†] B. J. Shappee [1] K. Auchettl [2,3] C. S. Kochanek [4,5] K. Z. Stanek,[4,5] W. P. Maksym [6] M. A. Tucker [4,5,7] M. E. Huber [1] N. Morrell [8] C. R. Burns [9] D. Hey [1] T. W.-S. Holoien [9] J. L. Prieto,[10,11] M. Stritzinger [12] A. Do [1] A. Polin [9,13,14] C. Ashall [15] P. J. Brown [16,17] J. M. DerKacy [15] L. Ferrari,[18,19] L. Galbany [20,21] E. Y. Hsiao [22] S. Kumar [23,22] J. Lu [24] and C. P. Stevens [15]

Affiliations are listed at the end of the paper

Accepted 2024 April 22. Received 2024 April 22; in original form 2024 January 10

ABSTRACT

We report the All-Sky Automated Survey for SuperNovae discovery of the tidal disruption event (TDE) ASASSN-23bd (AT 2023clx) in NGC 3799, a LINER galaxy with no evidence of strong active galactic nucleus (AGN) activity over the past decade. With a redshift of $z = 0.01107$ and a peak ultraviolet (UV)/optical luminosity of $(5.4 \pm 0.4) \times 10^{42}$ erg s^{-1}, ASASSN-23bd is the lowest-redshift and least-luminous TDE discovered to date. Spectroscopically, ASASSN-23bd shows H α and He I emission throughout its spectral time series, there are no coronal lines in its near-infrared spectrum, and the UV spectrum shows nitrogen lines without the strong carbon and magnesium lines typically seen for AGN. Fits to the rising ASAS-SN light curve show that ASASSN-23bd started to brighten on MJD 59988^{+1}_{-1}, ∼9 d before discovery, with a nearly linear rise in flux, peaking in the g band on MJD $60\,000^{+3}_{-3}$. Scaling relations and TDE light curve modelling find a black hole mass of $\sim 10^6$ M$_\odot$, which is on the lower end of supermassive black hole masses. ASASSN-23bd is a dim X-ray source, with an upper limit of $L_{0.3-10\,\mathrm{keV}} < 1.0 \times 10^{40}$ erg s^{-1} from stacking all *Swift* observations prior to MJD 60061, but with soft (∼0.1 keV) thermal emission with a luminosity of $L_{0.3-2\,\mathrm{keV}} \sim 4 \times 10^{39}$ erg s^{-1} in *XMM-Newton* observations on MJD 60095. The rapid ($t < 15$ d) light curve rise, low UV/optical luminosity, and a luminosity decline over 40 d of $\Delta L_{40} \approx -0.7$ dex make ASASSN-23bd one of the dimmest TDEs to date and a member of the growing 'Low Luminosity and Fast' class of TDEs.

Key words: accretion, accretion discs – black hole physics – transients: tidal disruption events.

1 INTRODUCTION

Tidal disruption events (TDEs) are the result of the partial or total disruption of a star passing near or within the tidal radius of a supermassive black hole (SMBH), leading to a luminous flare from accretion onto the SMBH (e.g. Rees 1988; Evans & Kochanek 1989; Phinney 1989; Ulmer 1999; Komossa 2015; Stone et al. 2019). Emission from TDEs occurs over a broad range of wavelengths, including the hard X-ray (e.g. Bloom et al. 2011; Burrows et al. 2011; Cenko et al. 2012b; Pasham et al. 2015), soft X-ray (e.g. Bade, Komossa & Dahlem 1996; Grupe, Thomas & Leighly 1999; Komossa & Greiner 1999; Auchettl, Guillochon & Ramirez-Ruiz 2017), ultraviolet (UV, e.g. Stern et al. 2004; Gezari et al. 2006, 2008, 2009), and optical bands (e.g. van Velzen et al. 2011; Cenko et al. 2012a; Gezari et al. 2012; Arcavi et al. 2014; Chornock et al. 2014; Holoien et al. 2014a, 2016a, b, 2019a, b; Vinkó et al. 2015; Brown et al. 2018). While active galactic nuclei (AGNs) probe actively accreting SMBHs, TDEs offer a rare opportunity to examine the activation of otherwise dormant SMBHs (e.g. Lodato & Rossi 2011; Guillochon & Ramirez-Ruiz 2015; Shiokawa et al. 2015; Metzger & Stone 2016). TDEs also provide a laboratory for studying shock physics (e.g. Lodato, King & Pringle 2009), jet formation (e.g. Farrar & Piran 2014; Wang & Liu 2016; Biehl et al. 2018), and the local environment and growth of SMBHs (e.g. Auchettl, Ramirez-Ruiz & Guillochon 2018; Jiang et al. 2021; Mockler et al. 2022).

However, the physics that underlies TDEs is complex. Possible parameters include the age, mass, composition, and rotation of the disrupted star (Kochanek 2016; Gallegos-Garcia, Law-Smith & Ramirez-Ruiz 2018; Golightly, Coughlin & Nixon 2019; Law-Smith, Guillochon & Ramirez-Ruiz 2019; Mockler, Guillochon & Ramirez-Ruiz 2019), the spin and mass of the SMBH (Ulmer 1999; Graham et al. 2001; Gafton & Rosswog 2019; Mockler et al. 2019), the stellar impact parameter (Guillochon & Ramirez-Ruiz 2013, 2015; Gafton & Rosswog 2019), the accretion fraction and viewing angle (Kochanek 1994; Lodato & Rossi 2011; Dai, McKinney & Miller 2015; Guillochon & Ramirez-Ruiz 2015; Shiokawa et al. 2015; Metzger & Stone 2016; Dai et al. 2018; Coughlin & Nixon 2019).

Despite all these parameters, optical and UV spectral energy distributions (SEDs) of TDEs are well modeled by blackbodies (e.g.

★ E-mail: willemh@hawaii.edu
† FINESST FI

Gezari et al. 2012; Holoien et al. 2014b, 2016a, b, 2018, 2019b, 2020; Brown et al. 2016; Hung et al. 2017; Leloudas et al. 2019; van Velzen et al. 2021; Hinkle et al. 2021c).

Several methods have been proposed to measure black hole mass from the TDE light curve (e.g. Ulmer 1999; Graham et al. 2001; Gafton & Rosswog 2019; Mockler et al. 2019; Ryu et al. 2020; Wen et al. 2020; Ramsden et al. 2022; Mummery et al. 2023; Sarin & Metzger 2024), these have been able to reproduce the known SMBH scaling relations with galaxy properties with varying success (e.g. Hammerstein et al. 2023). Finally, TDEs also show a Phillips (1993)-esque relationship between peak bolometric luminosity and decline rate (Hinkle et al. 2020, 2021c; Hammerstein et al. 2023).

From an optical spectroscopic perspective, the presence, strength and width of the observed lines vary (e.g. Arcavi et al. 2014; Hung et al. 2017; Leloudas et al. 2019; Wevers et al. 2019; Holoien et al. 2020; van Velzen et al. 2020; Charalampopoulos et al. 2023; Nicholl et al. 2022). Generally, optical emission lines are observed from hydrogen and/or helium, occasionally complemented by oxygen lines from Bowen fluorescence (e.g. Leloudas et al. 2019; van Velzen et al. 2020). Several potential theoretical explanations have been proposed to explain the variations in the spectra of TDEs, including photoionization physics (e.g. Gaskell & Rojas Lobos 2014; Guillochon, Manukian & Ramirez-Ruiz 2014; Roth et al. 2016; Kara et al. 2018; Leloudas et al. 2019), stellar composition differences (e.g. Kochanek 2016; Law-Smith et al. 2020; Mockler et al. 2022), and He star progenitors (e.g. Gezari et al. 2012; Strubbe & Murray 2015). While TDEs mostly have broad, Gaussian line profiles, some TDEs show line profiles with either strong, narrow line profiles (e.g. Holoien et al. 2020; van Velzen et al. 2020) or double peaks (e.g. Holoien et al. 2019a; Hung et al. 2020), which may be explained by the viewing geometry (e.g. Holoien et al. 2019a; Short et al. 2020; Hung et al. 2021). Finally, TDEs separate into diversely behaving spectral classes (Leloudas et al. 2019; van Velzen et al. 2021; Hammerstein et al. 2023), which has potential physical explanations that include partial versus complete disruption (Nicholl et al. 2022) and ionization from a shrinking photospheric radius (Charalampopoulos et al. 2023). However, a complete satisfactory explanation for the spectral classes is still needed. A larger sample of well-observed TDEs should advance our understanding of the underlying nature of TDEs and the SMBHs that cause them.

Fortunately, with many transient surveys currently operating such as the All-Sky Automated Survey for Supernovae (ASAS-SN; Shappee et al. 2014; Kochanek et al. 2017), the Asteroid Terrestrial Impact Last Alert System (ATLAS; Tonry et al. 2018a), the Panoramic Survey Telescope and Rapid Response System (Pan-STARRS; Chambers et al. 2016; Jones et al. 2021), and the Zwicky Transient Facility (ZTF; Bellm et al. 2019), more nuclear transients, including TDEs, are discovered each year, and a growing number are now found prior to peak brightness (e.g. Leloudas et al. 2019; Wevers et al. 2019; Holoien et al. 2019a, b, 2020; van Velzen et al. 2019b, 2020). The rising light curve and pre-maximum spectra provide important information about TDEs, such as the progression from a disrupted star to an accretion flow or an initial X-ray pulse (Carter & Luminet 1983; Brassart & Luminet 2008). The early detection of TDEs is especially important for a growing subclass of Faint and Fast (FaF) TDEs.[1] As their name suggests, the peak luminosity of a FaF TDE tends to be an order of magnitude less luminous combined with a rise and decline about twice as fast as a 'normal' TDE. Examples of FaF TDEs include iPTF16fnl (Blagorodnova et al. 2017; Brown et al. 2018), ATLAS18mlw (Hinkle et al. 2023), AT 2019qiz (Nicholl et al. w), AT 2020neh (Angus et al. 2022), and AT 2020wey (Charalampopoulos et al. 2023). While the observed sample is presently small, FaF TDEs may have a higher intrinsic rate than 'normal' TDEs (Charalampopoulos et al. 2023) but a lower discovery rate due to their lower luminosity. This is consistent with the findings of van Velzen (2018) and Yao et al. (2023) that TDEs have a steep luminosity function.

In addition to TDEs, transient sky surveys have uncovered additional classes of nuclear transients, including a number of ambiguous transients. For example, the differences between a TDE and single bright AGN flare are poorly understood (see Zabludoff et al. 2021 for a review), or, alternatively, changing-look AGN may originate from accretion rate changes caused by a TDE (e.g. Chan et al. 2019; van Velzen et al. 2020; Zhang 2021; Li et al. 2022; Ricci & Trakhtenbrot 2023). The potential for mistaken identification is particularly a problem for galaxies that already host AGN activity. In particular, another growing class of nuclear transients is ambiguous nuclear transients (ANTs), which exhibit observational characteristics seen in both AGNs and TDEs (e.g. Trakhtenbrot et al. 2019 Neustadt et al. 2020, Hinkle et al. 2022, Li et al. 2022, Holoien et al. 2022). While one may posit ANTs are merely TDEs in AGN hosts, some ANTs occur in host galaxies that lack active accretion (e.g. Malyali et al. 2021; Hinkle et al. 2022; Holoien et al. 2022).

Here, we present the discovery and follow-up observations of the nuclear transient ASASSN-23bd. We present the data in Section 2 and analysis in Section 3. Section 4 compares ASASSN-23bd with other FaF TDEs, and Section 5 summarizes the results.

2 DATA

2.1 Initial discovery and classification

ASAS-SN discovered ASASSN-23bd (a.k.a. AT 2023clx)[2] on MJD 59997.2 at (α, δ) = (11:40:09.397 + 15:19:38.54) in NGC 3799 using the Cassius unit in Chile (Stanek 2023). The ASAS-SN discovery g-band magnitude was 16.3, with a last non-detection on MJD 59988.3 at a limiting magnitude of $g \geq 17.9$. Taguchi et al. (2023) spectroscopically classified ASASSN-23bd as a TDE on MJD 60001.7.

The redshift of NGC 3799 is $z = 0.01107$ (Albareti et al. 2017), making ASASSN-23bd the lowest redshift TDE to date. Theureau et al. (2007) derive distance moduli of 33.6 ± 0.4 mag (∼51 Mpc; 21-cm line) and 35.6 ± 0.5 mag [∼134 Mpc; H-band Tully & Fisher (1977) relationship]. Assuming $H_0 = 73$ km s^{-1} Mpc^{-1} (Burns et al. 2018; Riess et al. 2022; Galbany et al. 2023), $\Omega_m = 0.3$, and $\Omega_\Lambda = 0.7$, the distance modulus to NGC 3799 is 33.50 ± 0.15 mag (50.1 ± 3.5 Mpc) in the cosmic microwave background frame. We adopt this distance.

2.2 Survey data

2.2.1 ASAS-SN light curve

ASAS-SN is a fully robotic survey with 20 14-cm telescopes distributed on five mounts at four sites, providing comprehensive all-sky monitoring with a cadence of ∼20 h (in good conditions) designed to detect nearby supernovae. The five ASAS-SN units are located at the Haleakala Observatory, the South African Astrophysical Observatory, the McDonald Observatory, and two at the

[1] In this context, faint refers to intrinsically faint, not observationally faint.

[2] https://www.wis-tns.org/object/2023clx

Table 1. Host-subtracted stacked ATLAS and ASAS-SN photometry of ASASSN-23bd.

JD	Filter	Magnitude	Uncertainty	Flux [mJy]	Uncertainty
$2459967.03^{0.01}_{0.01}$	*o*	20.297	99.999	−0.076	0.006
$2459970.14^{0.02}_{0.01}$	*o*	19.862	99.999	−0.068	0.008
$2459979.86^{0.03}_{0.04}$	*o*	19.325	99.999	−0.046	0.014

Uncertainties of 99.999 denote 3σ upper limits. Upper and lower uncertainties on the date of observation are derived during the stacking procedure to span the distance between the earliest and latest photometric epochs combined to result in that datum point. The full table will be available in the online journal.

Cerro Tololo Inter-American Observatory. The typical ASAS-SN observing strategy is to obtain three dithered images at each pointing. The ASAS-SN survey began observations in late 2011 with the *V* band. In 2017, ASAS-SN added 12 telescopes using the *g* band, and the original eight telescopes were switched from the *V* band to the *g* band in 2018.

ASAS-SN observed the location of ASASSN-23bd 3441 times before discovery, and all images were reduced using the standard ASAS-SN pipeline based on the ISIS image subtraction package (Alard & Lupton 1998; Alard 2000). We used images taken before MJD 59 800 to construct the reference image, removing any images with a large FWHM ($\geq$1.7 pixels), a 3σ depth that was too shallow ($g < 17.0$ mag), or that showed signs of cirrus or clouds.

Similar to the standard ASAS-SN Sky Patrol photometry (Kochanek et al. 2017; Hart et al. 2023), we use the IRAF APPHOT package with a 2-pixel (16 arcsec) radius to perform aperture photometry on each subtracted image, generating a differential light curve. The photometry is calibrated using the AAVSO Photometric All-Sky Survey (Henden et al. 2015). We then stack the individual ASAS-SN images on different time scales for different parts of the light curve. First, when looking for pre-discovery variability we stack the dithered images together. Next, from 40 d before to 25 d after discovery, we stack in 25-h bins to cover the rapid rise and decline. Lastly, for the declining light curve, we stack in 100-h bins to better follow the relatively slow fading. The ASAS-SN photometric observations are compiled in Table 1.

2.2.2 *ATLAS light curve*

The ATLAS survey primarily focuses on detecting small asteroids that have a chance of terrestrial collision using two filters: a cyan (*c*; 420–650 nm) filter and an orange (*o*; 560–820nm) filter (Tonry et al. 2018a). ATLAS uses 0.5 m Wright-Schmidt telescopes in Hawaii, Chile, and South Africa to obtain four 30-s exposures in an hour-long window for 200–250 fields per night, covering approximately a quarter of the sky (Smith et al. 2020). Data were retrieved from the ATLAS Transient Science Server (Smith et al. 2020). The ATLAS light curve contains 2527 images, with the earliest on MJD 57400.6. We combined the four nightly ATLAS images to derive a light curve with 630 epochs. The initial rise was observed in the ATLAS *o* band, whereas the peak was observed in the ATLAS *c* band. Data taken on the same night were stacked using a weighted average, excluding data affected by clouds. The ATLAS photometric observations are also compiled in Table 1.

2.2.3 *TESS data*

NGC 3799 was observed by the Transiting Exoplanet Survey Satellite (TESS; Ricker et al. 2015) in sectors 22, 45, 46, and 49. Unfortunately, these sectors all occurred before the discovery of ASASSN-23bd. We reduced the TESS data in a similar manner to the ASAS-SN data following the processes detailed in Vallely et al. (2019, 2021), and Fausnaugh et al. (2021). We used the ISIS package (Alard & Lupton 1998; Alard 2000) to image subtract the full-frame TESS images. Median filters were used to remove artifacts like CCD straps. We produced light curves from these subtracted images with reference images constructed on a per-sector basis using the first 100 good-quality full-frame images without compromised pointing, significant scattered light, or data quality flags. For the extended mission with its shorter integration times, we use the first 300 images that meet these criteria.

2.2.4 *ZTF light curve*

ZTF uses the Samuel Oschin 48-in Schmidt telescope at the Palomar Observatory and a camera with a 47 deg^2 field of view to obtain images as deep as 20.5 *r*-band mag in 30-s exposures. ZTF observed the field containing ASASSN-23bd starting on MJD 58202.3. We use the ZTF *g*- and *r*-band light curves between MJD 58202.3 and MJD 60 090 obtained through the ZTF forced photometry service.[3] These light curves have 673 *g*- and *r*-band epochs constructed from 1726 images. Following the ASAS-SN discovery announcement, ZTF reported a detection at $g = 19.28$ mag on MJD ∼59980 to TNS; however, our analysis of the ZTF forced photometry does not show a detection at this epoch. All the ZTF detections are after the peak of ASASSN-23bd. Since higher-cadence data are available from the *Swope Telescope*, as discussed below, we only include the ZTF data in our analysis of previous AGN variability.

2.3 Follow-up observations

2.3.1 *Swope observations*

As part of the Precision Observations of Infant Supernova Explosions (POISE; Burns et al. 2021) collaboration, we obtained follow-up images from the 1.0-m Henrietta Swope Telescope. These data were taken in the Carnegie Supernova Project (CSP) natural system for which the *BV* photometry is calibrated using standards from Landolt (2007) and the *gri* photometry is calibrated using standards from Smith et al. (2002). These standards are converted to the CSP system using colour terms from Krisciunas et al. (2017) and Phillips et al. (2019). For more information on the CSP filter system, see Stritzinger et al. (2011) and references therein.

The Swope photometry is template-subtracted using Pan-STARRS (Chambers et al. 2016) imaging data. Calibration is done using RefCat2 (Tonry et al. 2018b) magnitudes transformed to the CSP natural system using the colour terms found in Krisciunas et al. (2017) and Phillips et al. (2019). Finally, we use the corrections listed on the CSP website[4] to convert to the AB system.

[3] https://irsa.ipac.caltech.edu/Missions/ztf.html.
[4] https://csp.obs.carnegiescience.edu/data/filters

Table 2. Host-subtracted photometry of ASASSN-23bd from *Swift* and Swope.

JD	Filter	Magnitude	Uncertainty
2460003.25	*U*	16.42	0.06
2460003.25	*w*1	16.79	0.07
2460003.26	*m*2	16.88	0.05

The full table will be available in the online journal. The *B* and *V* filter keys correspond to Swope filters.

2.3.2 Swift *observations*

The Neil Gehrels Swift Observatory (*Swift*; Gehrels et al. 2004) acquired 19 epochs of data between MJD 60 000 and MJD 60 061 (PIs: Leloudas, Gomez, Huang, and Wevers). *Swift* simultaneously observed ASASSN-23bd with the UltraViolet and Optical Telescope (UVOT; Roming et al. 2005) and X-Ray Telescope (XRT; Burrows et al. 2005). The *Swift* data through MJD 60 061 are included here; later *Swift* observations exist, but these data are too noisy to be useful.

All exposures for each UVOT epoch were combined using the HEASOFT version 6.31.1 UVOTIMSUM package, and aperture photometry was obtained using the UVOTSOURCE package. An aperture of 5 arcmin is used for both the source and the background. Stacked archival *Swift* host-galaxy images were subtracted in all bands except the *B* band, which lacks archival *Swift* imaging of the host. We compute Vega-system magnitudes using the Breeveld et al. (2011) zero points, which update the Poole et al. (2008) zero points. A comparison to photometry from the Swift Optical/Ultraviolet Supernova Archive (SOUSA; Brown et al. 2014) pipeline yields similar photometry to ours. Finally, the magnitudes are converted to AB magnitudes.[5]

Due to the lack of archival *B*-band observations, the large *V*-band uncertainties at late times, and the existence of high quality *B* and *V* data from POISE, we elect not to show the *Swift B*- or *V*-band photometry nor use the *Swift B*-band photometry in our analysis. The *Swift V*-band photometry is included in the blackbody/SED fits. The Swope and *Swift* photometry is compiled in Table 2.

The *Swift* XRT data was collected in photon-counting mode. Using the most up-to-date calibrations and the standard filters and screenings, the observations were processed using the XRTPIPELINE version 0.13.7. Using a source region with a radius of 47 arcmin centred on the location of ASASSN-23bd and a source-free background region with a radius of 150 arcmin centred at $(\alpha, \delta) = (11{:}39{:}56.13, +15{:}22{:}23.90)$, no significant X-ray emission associated with the source was found in the individual epochs.

To constrain the X-ray emission, we merged all 19 observations (up to ObsID sw00015897021 on MJD $= 60061$) using the HEASOFT tool XSELECT version 2.5b to derive a 3σ upper limit of 1×10^{-3} counts s^{-1} for the 0.3–10.0 keV energy range. Assuming an absorbed power law with a Galactic column density of 2.5×10^{20} cm^{-2} (HI4PI Collaboration 2016) and a photon index of 2 at the redshift of the host galaxy, we obtain an absorbed flux limit of $<3.5 \times 10^{-14}$ erg cm^{-2} s^{-1}, which corresponds to an X-ray luminosity limit of $<1 \times 10^{40}$ erg s^{-1}. If we assume an absorbed blackbody model with a temperature of 0.1 keV and a host column density of 1×10^{20} cm^{-2}, as derived in Section 2.3.3, we obtain an unabsorbed flux limit of $<2.7 \times 10^{-14}$ erg cm^{-2} s^{-1}, which corresponds to an X-ray luminosity of $<7.9 \times 10^{39}$ erg s^{-1}

[5]The conversions are found at https://swift.gsfc.nasa.gov/analysis/uvot_digest/zeropts.html

2.3.3 XMM-newton

XMM-Newton targeted ASASSN-23bd through joint time awarded as part of the Hubble GO program 16 775 (PI: Maksym). XMM-Newton observed NGC 3799 on 2023 May 31 (MJD 60095; obsid 0892201601) for 15 ks, of which 11.8 ks were useful. ASASSN-23bd was detected at $\sim 10\sigma$ with $\sim$170 counts (maximum likelihood 185 from the EPIC detection pipeline). As a first test, we extracted the PN counts from a $r = 30$ arcsec region centred on the source and from a $r = 30$ arcsec sourceless background region near the NW corner of the same PN CCD, avoiding the chip edges. The PN 2.0–10.0 keV excess had $<2\sigma$ significance, with ~ 90 per cent of the photons observed in the 0.1–2 keV band. Of these, only 1 net count was found between 1.0–2.0 keV. For a first estimate of spectral properties, we used PIMMS[6] to estimate a blackbody temperature assuming a host column density of 1×10^{20} cm^{-2}, scaling from our derived host extinction limit ($A_V \leq 0.05$; see Section 3.1) and Galactic extinction ($A_V = 0.085$; Schlafly & Finkbeiner 2011) from `colden`[7] The model blackbody temperature was iteratively increased in steps of 0.01 keV to match the observed hardness ratio such that HR = (H-S)/(H + S) $= -0.38$ where S = 0.2–0.5 keV and H = 0.5–1.0 keV. This leads to a blackbody temperature estimate of $kT \sim 0.09$ keV. This leads to an observed flux of $\sim 8.8 \times 10^{-15}$ erg s^{-1} cm^{-2} in the Swift 0.3–10 keV band, or an intrinsic $\sim 4.2 \times 10^{39}$ erg s^{-1} for an unabsorbed blackbody in the 0.1–2 keV band. It is undetected in the hard band ($<1.3 \times 10^{-14}$ erg s^{-1} cm^{-2} at 3σ in the 2–10 keV band assuming a $\Gamma = 1.7$ power law). To check our assumptions, we also extracted a spectrum with `XMM SAS`[8] and fit it with XSPec[9] using 10-count bins and `lstat` as the minimization statistic. The blackbody fit produces $kT = 0.10 \pm 0.02$, $n_H < 1.1 \times 10^{21}$cm^{-2}, and $F_{0.3-10\,\mathrm{keV}} = [1.53 \pm 0.27] \times 10^{-14}$erg s^{-1}cm^{-2} (absorbed) and $[3.17 \pm 1.85] \times 10^{-14}$erg s^{-1}cm^{-2} (unabsorbed; 90 per cent confidence), with χ^2/degrees of freedom = 40.32/25. A complete analysis of the XMM-Newton data will be presented in Maksym et al. (in preparation).

2.3.4 *Spectroscopic observations*

We acquired 24 spectra of ASASSN-23bd between MJD 60 007 and MJD 60 075 and also include two public spectra of ASASSN-23bd accessed through the Transient Name Server (TNS) and a public *HST* spectrum. The first TNS spectrum[10] was taken on the Seimi telescope using the Kyoto Okayama Optical Low-dispersion Spectrograph Integral Field Unit (KOOLS-IFU; Matsubayashi et al. 2019). The second TNS spectrum[11] was taken on the Keck-I telescope using the Low-Resolution Imaging Spectrometer (LRIS; Oke et al. 1995; Rockosi et al. 2010) and reported by Johansson et al. (2023).

Our optical spectroscopic observations of ASASSN-23bd are from the POISE (Burns et al. 2021) and SCAT (Tucker et al. 2022) collaborations. POISE observations were taken using the Inamori-Magellan Areal Camera and Spectrograph (IMACS; Dressler et al. 2006) on the 6.5-m *Magellan Baade* telescope. SCAT observations were taken using the University of *Hawaii* 2.2-m telescope (UH2.2) on Mauna Kea using the Supernova Integral Field Spectrograph (SNIFS; Lantz et al. 2004) and on the *Australian National University*

[6]https://cxc.harvard.edu/toolkit/pimms.jsp
[7]https://cxc.harvard.edu/toolkit/colden.jsp
[8]https://www.cosmos.esa.int/web/xmm-newton/sas
[9]https://heasarc.gsfc.nasa.gov/xanadu/xspec/
[10]Accessed via https://www.wis-tns.org/object/2023clx
[11]Accessed via https://www.wis-tns.org/object/2018meh

Table 3. Log of spectroscopic observations.

UT Date	MJD [d]	Epoch [d]	Telescope	Spectrograph
2023-02-26	60001.6	4.4	Seimi	KOOLS-IFU
2023-03-04	60007.5	10.3	SS2.3	WiFeS
2023-03-05	60008.3	11.1	Baade	IMACS
2023-03-14	60017.5	20.3	SS2.3	WiFeS
2023-03-15	60018.3	21.1	Baade	IMACS
2023-03-17	60020.5	23.3	SS2.3	WiFeS
2023-03-19	60022.5	25.3	SS2.3	WiFeS
2023-03-20	60023.3	26.1	Baade	IMACS
2023-03-20	60023.5	26.3	Keck1	LRIS
2023-03-21	60024.6	27.4	SS2.3	WiFeS
2023-03-27	60030.4	33.2	UH2.2	SNIFS
2023-03-28	60031.4	34.2	UH2.2	SNIFS
2023-03-29	60032.4	35.2	UH2.2	SNIFS
2023-03-29	60032.5	35.3	SS2.3	WiFeS
2023-04-05	60039.5	42.3	SS2.3	WiFeS
2023-04-10	60044.4	47.2	UH2.2	SNIFS
2023-04-11	60045.4	48.2	UH2.2	SNIFS
2023-04-13	60047.2	50.0	Baade	IMACS
2023-04-14	60048.4	51.2	SS2.3	WiFeS
2023-04-16	60050.4	53.2	UH2.2	SNIFS
2023-04-21	60055.4	58.2	UH2.2	SNIFS
2023-04-21	60055.5	58.3	SS2.3	WiFeS
2023-04-24	60058.4	61.2	UH2.2	SNIFS
2023-04-28	60062.3	65.1	UH2.2	SNIFS
2023-05-10	60074.4	77.2	UH2.2	SNIFS
2023-03-26	60029.4	32.2	IRTF	SpeX
2023-04-04	60038.9	41.7	HST	STIS

The epoch phase is relative to the time of discovery on MJD 59997.2

2.3-m telescope (SS2.3) using the Wide-Field Spectrograph (WiFeS; Dopita et al. 2007, 2010).

Data reduction for IMACS was performed using standard IRAF[12] packages and uses the methods described in Hamuy et al. (2006) and Folatelli et al. (2013). SNIFS spectra were reduced using the SCAT pipeline described in Tucker et al. (2022), and WiFeS spectra were reduced using standard procedures implemented in PyWiFeS (Childress et al. 2014).

Further spectral data were taken using NASA's InfraRed Telescope Facility (IRTF) with SpeX (Rayner et al. 2003) as part of IRTF program 2023A060 (PI: Hinkle) and *HST* data were taken with the Space Telescope Imaging Spectrograph (STIS; Woodgate et al. 1998) as part of GO program 16 775 (PI: Maksym). The SpeX data were reduced with telluric corrections from an A0V star using the standard SpeXtool procedures described in Cushing, Vacca & Rayner (2004), and the reduced STIS spectrum was obtained through the Mikulski Archive for Space Telescopes. Table 3 presents a log of the spectroscopic observations of ASASSN-23bd.

3 ANALYSIS

In this section, we analyse the archival host properties of NGC 3799. We search for previous AGN-like variability and compute the general host-galaxy properties. Additionally, we fit the rising light curve of ASASSN-23bd with single- and double-component models and perform blackbody fits to the photometry. Finally, we analyse the optical spectral time series, especially the evolution of the full width at half-maximum (FWHM) and luminosity of the H α feature.

3.1 Archival observations of host galaxy NGC 3799

NGC 3799 is a well-observed galaxy morphologically classified as a SB(s)b:pec (de Vaucouleurs et al. 1991) galaxy. It is designated as a peculiar galaxy because it is interacting with NGC 3800. There is evidence that galaxies that have undergone recent mergers may be more likely to host a TDE (Prieto et al. 2016; Hammerstein et al. 2021). NGC 3799 is a Low Ionization Nuclear Emission Line Region (LINER) AGN (Toba et al. 2014). The archival SDSS spectrum (York et al. 2000) shows H β, Mg b λ5175, Na I D $\lambda\lambda$5890, 5896, and Ca II KHG $\lambda\lambda$3934, 3968, 4308, Ca II $\lambda\lambda$8542, 8662, and Mg I λ8807 absorption and [O III] $\lambda\lambda$4959,5007, [N II] λ6584, [S II] $\lambda\lambda$6717, 6731, and H α emission.

Fig. 1 compares NGC 3799 with the host galaxies of Broad H/He TDEs and the spectroscopic properties of SDSS DR8 (Eisenstein et al. 2011) galaxies from Brinchmann et al. (2004). The top left panel shows the equivalent width (EW) of H α and the Lick H δ_A absorption index. H α is a current star-formation indicator, while the Lick H δ_A absorption index provides information about the past Gyr of star formation to identify post-starburst galaxies. The boxes are from French, Arcavi & Zabludoff (2016) and indicate the host galaxy's evolutionary stage. TDEs generally prefer E + A or peculiar host galaxies (Arcavi et al. 2014; French et al. 2016; Hammerstein et al. 2021), but because TDEs can occur in much fainter galaxies than SDSS can obtain spectra for, a complete picture of TDE host properties requires a correction for the difference in the flux limit (see e.g. Hammerstein et al. 2021) that is not used in this work.

The top right panel shows the H α EW and $\log_{10}$([N II]/H α), which helps to discriminate between ionization mechanisms, especially those of LINER galaxies (Cid Fernandes et al. 2011). The bottom left panel of Fig. 1 shows a galaxy diagnostic based on $\log_{10}$([O III]/H β) and $\log_{10}$([N II]/H α), and the bottom right shows another one using $\log_{10}$([O III]/H β) and $\log_{10}$([S II]/H α) (Baldwin, Phillips & Terlevich 1981; Veilleux & Osterbrock 1987). The numerical values for each parameter are $EW_{\mathrm{H}\alpha} = 3.03 \pm 0.13$ Å, $EW_{\mathrm{H}\delta_A} = 0.58 \pm 0.41$ Å, $\log_{10}([\mathrm{N\,II}]/\mathrm{H}\alpha) = -0.071 \pm 0.021$, $\log_{10}([\mathrm{S\,II}]/\mathrm{H}\alpha) = -0.233 \pm 0.032$, and $\log_{10}([\mathrm{O\,III}]/\mathrm{H}\beta) = 0.215 \pm 0.042$. Finally, we note that NGC 3799 has a $W1 - W2$ colour of -0.03 mag, which indicates no strong AGN activity (Stern et al. 2012). In summary, Fig. 1 shows NGC 3799 is still undergoing star formation and hosts weak AGN activity.

We use the photometry in Table 4 to estimate several host-galaxy parameters using the Fitting and Assessment of Synthetic Templates package (FAST; Kriek et al. 2009). We assume a Salpeter (1955) initial mass function, an exponentially declining star-formation rate, and the stellar population models of Bruzual & Charlot (2003). This population model uses light from the entire host galaxy. However, there is evidence for an older, quiescent nucleus from the SDSS and Pan-STARRS host-galaxy images. The star formation is likely associated with the spiral arms and driven by NGC 3799's tidal interactions with its larger nearby neighbour, NGC 3800. The model results give an age of $2.0^{+0.2}_{-0.4}$ Gyr, a stellar mass of $6.3^{+0.6}_{-0.6} \times 10^9$ $\mathrm{M}_\odot$, a star formation rate of $1.2^{+0.1}_{-0.6} \times 10^{-1}$ $\mathrm{M}_\odot$ yr^{-1}, and a specific star formation rate of $2.5^{+1.3}_{-0.3} \times 10^{-11}$ yr^{-1}. For the Reines & Volonteri (2015) scaling relation, the host stellar mass implies a black hole mass of $M_{\mathrm{BH}} = (1.6 \pm 1.0) \times 10^6$ $\mathrm{M}_\odot$, which is similar to other FaF

[12]The Image Reduction and Analysis Facility (IRAF) is distributed by the National Optical Astronomy Observatory, which is operated by the Association of Universities for Research in Astronomy, Inc., under cooperative agreement with the National Science Foundation.

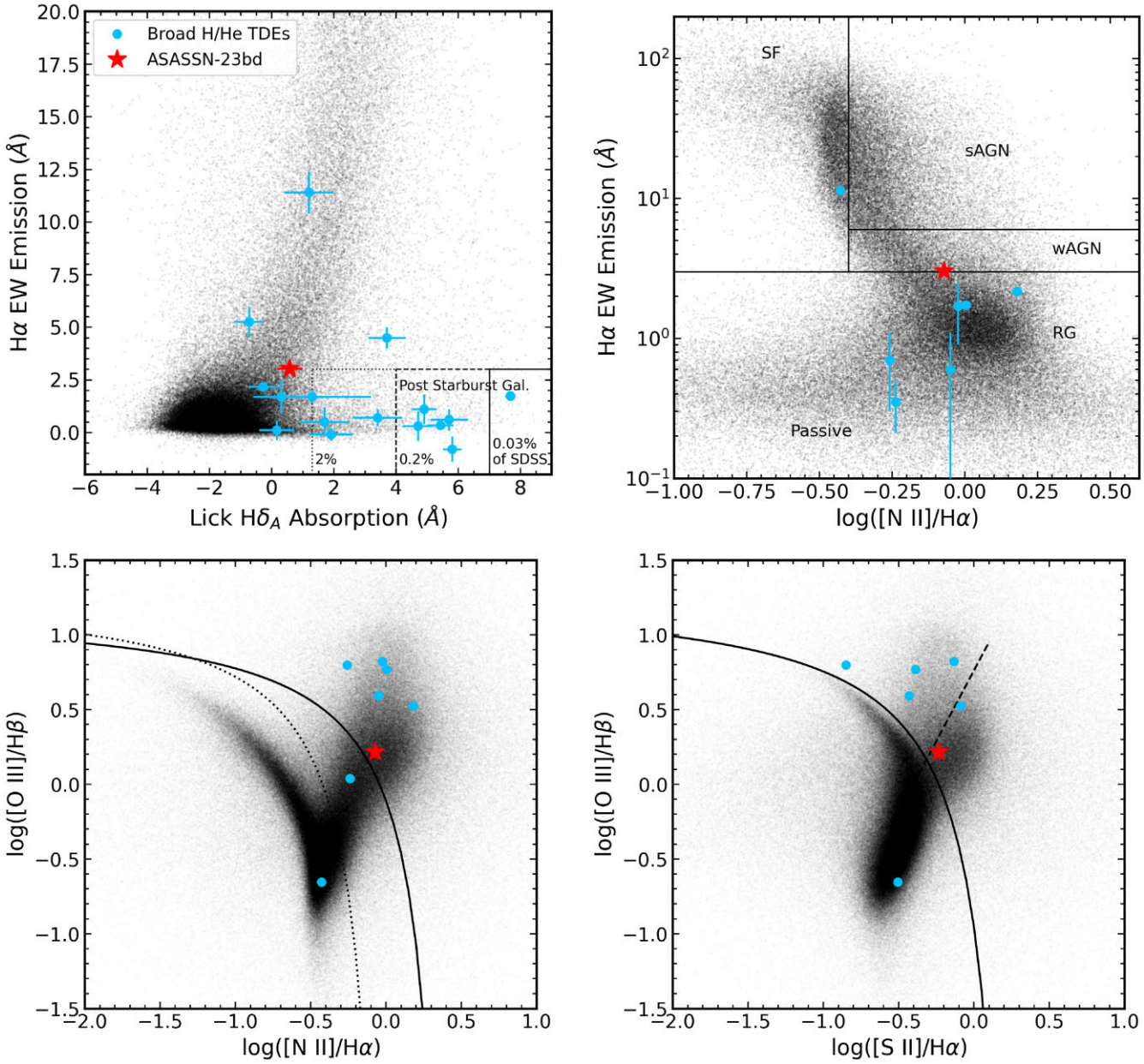

Figure 1. Host galaxy properties for selected broad H/He TDEs (circles) and ASASSN-23bd (star). Black background points are galaxies from SDSS DR8 (Eisenstein et al. 2011) in the MPA-JHU catalogue (Brinchmann et al. 2004). *Upper Left Panel:* EW of the host galaxy H α and the Lick H δ_A absorption index. H α traces current star formation whereas the Lick H δ_A traces the star formation in the past Gyr. The uncertainty for NGC 3799 is the size of the marker. *Upper Right Panel:* H α EW and $\log_{10}$([N II]/H α). Sometimes called the WHAN diagram (Cid Fernandes et al. 2011). Plotted lines separate regions corresponding to star-forming galaxies (SF), strong AGN (sAGN), weak AGN (wAGN), and 'retired galaxies' (RG). *Lower Left Panel:* $\log_{10}$([O III]/H β) and $\log_{10}$([N II]/H α) lines (Baldwin et al. 1981; Veilleux & Osterbrock 1987). The solid line separates AGNs (above the line) and H II regions (below the line; Kewley et al. 2001). Objects between the solid and dotted line are considered composite objects. *Lower Right Panel:* $\log_{10}$([O III]/H β) and $\log_{10}$([S II]/H α) (Veilleux & Osterbrock 1987). The AGN region lies above the solid line and H II regions lie below the line. The dashed line is a theoretical separation between Seyferts, located above and to the left, and LINERS, located below and to the right (Kewley et al. 2006).

TDEs (e.g. Charalampopoulos et al. 2023 and Blagorodnova et al. 2017).

Since NGC 3799 is classified as a LINER, we searched for prior X-ray emission that could indicate possible AGN activity using archival *Swift* XRT observations obtained before ASASSN-23bd. We find no evidence of prior X-ray emission from the host. Merging all available archival observations, we obtain a 3σ upper limit to the 0.3–10.0 keV count rate of 0.002 counts s^{-1}. Assuming an absorbed power law with a photon index $\Gamma = 1.7$ (e.g. Ricci et al. 2017) and a Galactic column density of 2.51×10^{20} cm^{-2} (HI4PI Collaboration 2016), we derive an absorbed luminosity of $<2 \times 10^{40}$ erg s^{-1}. This limit rules out strong, but not weak, AGN activity, consistent with Fig. 1.

It appears that ASASSN-23bd is not significantly affected by extinction. The Milky-Way extinction towards NGC 3799 is $A_V = 0.085$ mag (Schlafly & Finkbeiner 2011). We use four different methods to estimate the host-galaxy extinction. First, the pseudo-EW

Table 4. Archival photometry of NGC 3799 from Swift (UVW2, UVM2, UVW1; Gehrels et al. 2004; Poole et al. 2008; Breeveld et al. 2011), SDSS (*u*, *g*, *r*, *i*, *z*; Aguado et al. 2019), 2MASS (J, H, K_s; Skrutskie et al. 2006), and WISE (W1 and W2; Wright et al. 2010).

Filter	Magnitude	Magnitude uncertainty
UVW2	16.57	0.02
UVM2	16.89	0.03
UVW1	16.31	0.02
u	15.60	0.01
g	14.23	0.01
r	13.71	0.01
i	13.41	0.01
z	13.25	0.01
J	12.90	0.03
H	12.80	0.04
K_s	12.95	0.04
W1	14.27	0.02
W2	14.94	0.02

All photometry is in the AB system.

of the Na I D line in the SDSS spectrum can be used to estimate an extinction using the relationship of Poznanski, Prochaska & Bloom (2012). We perform a 1500 iteration bootstrap on the Na I D line and take the median of the 1500 resulting extinction values to derive $A_V = 0.55 \pm 0.09$ mag. Secondly, the FAST fit provides an extinction estimate of $A_V = 0.09^{+0.36}_{-0.01}$ mag. Thirdly, using the SDSS line fluxes, the Balmer decrement is 3.7 ± 0.3. Using the Balmer decrement–extinction relationship from Domínguez et al. (2013), we derive $E(B-V) = 0.22$ mag and $A_V = 0.88$ mag, although with $R_V = 3.1$, this drops to $A_V = 0.66$ mag. However, these estimates may be inaccurate for several reasons. First, they are derived using emission from the larger narrow-line region and thus may overestimate the line-of-sight extinction toward the nucleus. Secondly, the FAST population model integrates emission from the whole galaxy, but there is evidence for an older, quiescent nucleus with star formation associated with the spiral arms and possible tidal interactions with its larger nearby neighbour, NGC 3800. Thirdly, the Balmer decrement assumes Case B recombination as the only source of H-line production. But NGC 3799 is a LINER, implying that shocks may modify the line ratios, flattening the Balmer decrement and reducing the extinction estimate. This is difficult to disentangle from the effects of dust. There is no significant Na I D line in our follow-up spectra where the nuclear transient dominates the emission, although Charalampopoulos et al. (2024) report Na I D in their spectroscopic data. However, we find the upper limit on Na I D absorption from the LRIS spectrum corresponds to $A_V \leq 0.05$ mag. This is a line-of-site estimate directly from the TDE observations, so we assume that the host-galaxy extinction of ASASSN-23bd is negligible.

Since NGC 3799 hosts weak AGN activity, we searched the archival ASAS-SN, ATLAS, ZTF, and TESS observations for AGN variability or outbursts prior to ASASSN-23bd. The forced-photometry light curves are shown in Fig. 2 and show no evidence of variability. We find that the RMS is ≤100 μJy in each TESS sector, with sectors 22 and 49 having the largest RMS at 90 μJy. The ATLAS *o* band has the largest RMS variance out of all the survey data with a value of 263 μJy, corresponding to a luminosity of $\nu L_\nu = 3.6 \times 10^{41}$ erg s^{-1}. If this were real and corresponded to a 1 per cent variability amplitude, then the AGN has $\nu L_\nu < 3.6 \times 10^{43}$ erg s^{-1}. With such low variance, we rule out strong AGN activity with $\nu L_\nu > 10^{41}$ erg s^{-1} over the past decade.

3.2 Photometric analysis

Fig. 3 presents our photometric data for ASASSN-23bd. To constrain the time of peak, we perform Markov-Chain Monte Carlo (MCMC) fits with a simple parabolic model to the ASAS-SN data near peak to find $t_{\rm peak}({\rm MJD}) = 60\,000^{+3}_{-3}$.

Yao et al. (2023) fit the rising light curves of 33 TDEs and find that a power-law fit is preferential to a Gaussian fit. Thus, we fit the rising ASAS-SN *g*-band photometry with two different power-law models of the form

$$f(t) = \begin{cases} f_0 & t < t_0 \\ f_0 + k\left(\frac{t-t_0}{1+z}\right)^a & t \geq t_0. \end{cases} \quad (1)$$

where

$$k \equiv \frac{h}{(1+z)^2}. \quad (2)$$

and α is either a constant, single-power model as in Vallely et al. (2021) and Hinkle et al. (2021b) or

$$\alpha \equiv \alpha_1 \left(1 + \frac{\alpha_2(t-t_0)}{(1+z)}\right) \quad (3)$$

as also used in Vallely et al. (2021). While the value of α in the one-component model is sensitive to how much of the rising light curve is fit (e.g. Vallely et al. 2019, 2021), the α_1 parameter from the two-component model is not. We use the emcee fitting package (Foreman-Mackey et al. 2013) with the results given in Table 5 and shown in Fig. 4. The two models produce consistent results for f_0, h, t_0, and α/α_1. In both models, the power-law slope of the rise is closer to linear in time than quadratic. The two-component model can also be used to determine the peak *g*-band magnitude. The median peak value is 1.09 ± 0.09 mJy, corresponding to an AB magnitude of 16.30 ± 0.03.

To estimate the theoretical properties of ASASSN-23bd, we fit our host-subtracted light curves using the Modular Open Source Fitter for Transients package (MOSFiT; Guillochon et al. 2017; Mockler et al. 2019). MOSFiT provides estimates of the physical properties of the star, the SMBH, and the encounter between the star and SMBH by generating bolometric light curves from predefined TDE models, subsequently deriving light curves for each photometric band, and finally fitting the derived light curves to the observed ones. The MOSFiT results are tabulated in Table 6. The SMBH mass from these fits agrees well with the mass estimate from the host-galaxy scaling relationships presented in Section 3.1.

We fit a blackbody model to the optical and UV data. Fig. 5 shows the resulting temperature, luminosity, and radius, and Fig. 6 shows the best-fit blackbody at the epoch of the NIR spectrum. We only correct for the effects of the Milky Way extinction and do not include the host-galaxy extinction since it appears to be negligible [although Charalampopoulos et al. (2024) argue for a significant host-galaxy extinction component]. The results show a nearly constant blackbody temperature and radius and a decreasing blackbody luminosity with time. Our blackbody fits are consistent with the fits performed by Zhu et al. (2023) using SUPERBOL (Nicholl 2018).

Fig.7 shows a smoothed, 3-colour image of the *XMM-Newton* detection created using the standard pipeline bands for ETRUECOLOUR[13] The *XMM-Newton* data implies a blackbody with $L \approx 4 \times 10^{39}$ erg s^{-1} and $kT = 0.1$ keV, and thus, a (spherical) photospheric radius of $\sim 1.8 \times 10^9$ cm (see Section 2.3.3), which is much smaller than the Schwarzschild radius for a $10^6\ M_\odot$ SMBH of $\sim 3.0 \times 10^{12}$ cm.

[13] https://heasarc.gsfc.nasa.gov/docs/xmm/sas/USG/etruecolour.html

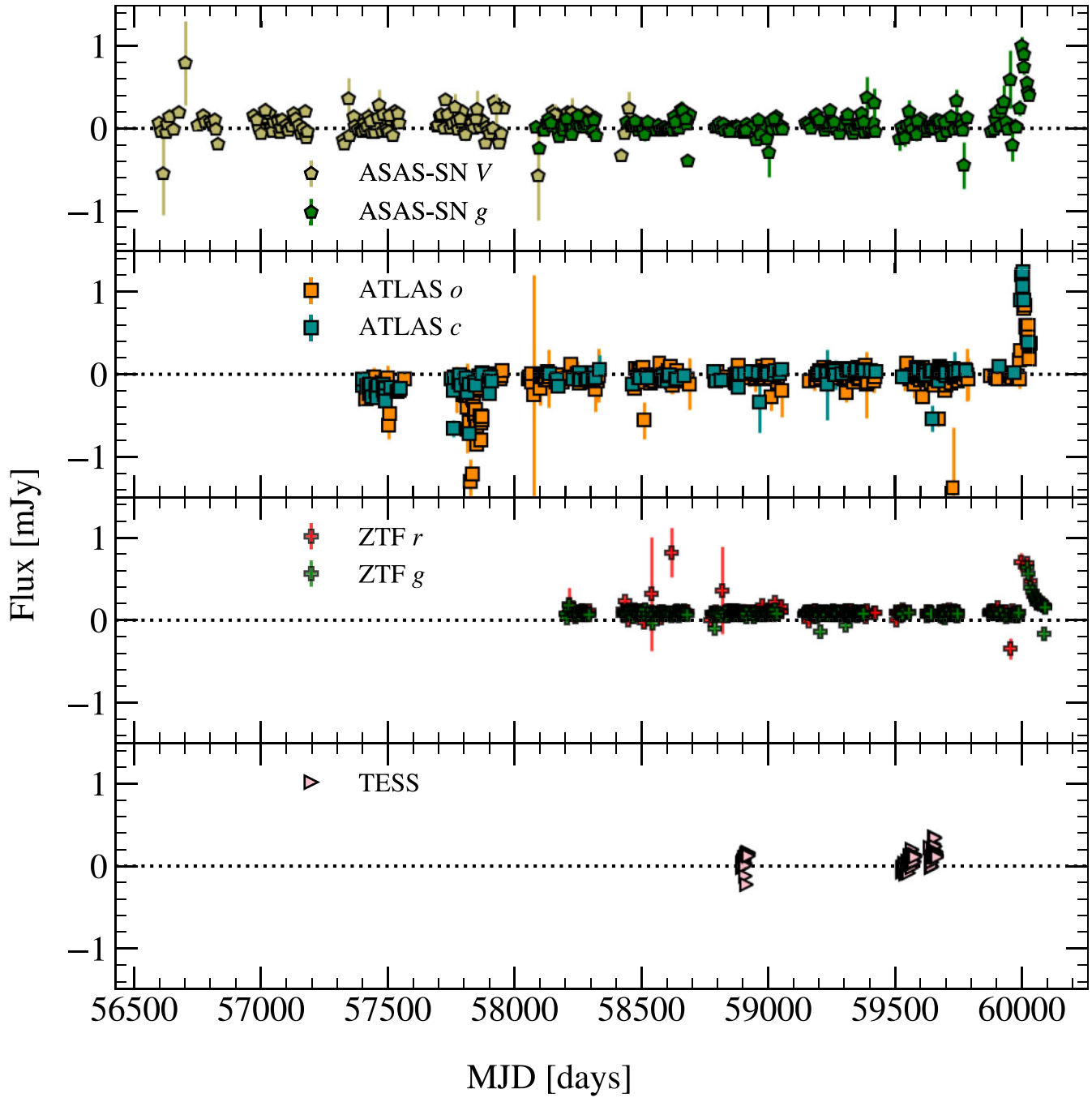

Figure 2. Stacked archival flux light curves for NGC 3799 with 3σ uncertainties. There are no prior AGN flares detected in NGC 3799. The ASAS-SN *V*- and *g*-band data are the khaki and green pentagons, respectively; the ZTF *g*- and *r*-band data are the green and red plusses, respectively; the TESS data are pink triangles; and the ATLAS *c*- and *o*-band data are cyan orange squares, respectively. The ATLAS data near MJD 57 800 pass reasonable ATLAS quality cuts but may nonetheless be adversely affected from clouds.

An unphysically small blackbody radius for the X-ray emission is a common occurrence in TDEs (e.g. Brown et al. 2017; Hinkle et al. 2022). Mummery (2021) showed that assuming a single-temperature, spherical blackbody can underestimate the TDE accretion disc size by up to an order of magnitude.

3.3 Spectroscopic analysis

The optical spectra of ASASSN-23bd are presented in Fig. 8. We photometrically calibrated (also known as colour matching or 'mangling'; Hsiao et al. 2007) the spectra using the optical photometry from POISE. Synthetic fluxes were calculated from each spectrum and compared to the POISE fluxes. The flux ratios are fit by a spline, which is then used to correct the spectrum. This process is repeated until the synthetic fluxes agree with the POISE fluxes. Our NIR spectrum is presented in Fig. 9 where no mangling was applied. ASASSN-23bd lacks the NIR spectral features commonly observed in AGNs such as H, He, or coronal emission lines. The lack of coronal lines seems to require having little nuclear gas. We fit a power law of the form $F_\lambda = a \times \lambda^b + c$ to our NIR spectrum. The

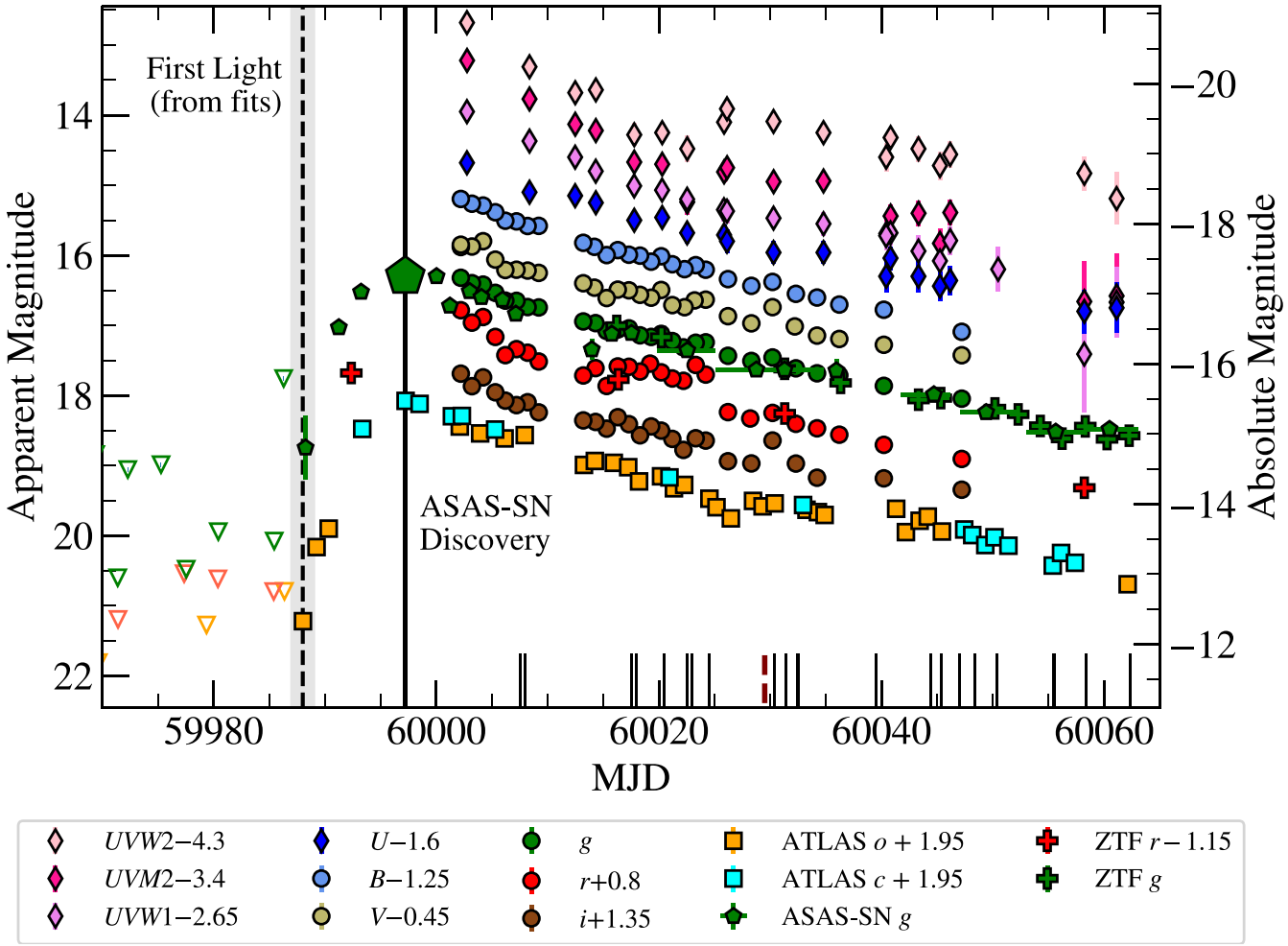

Figure 3. Ultraviolet and optical light curves of ASASSN-23bd from *Swift* (diamonds), Swope (circles), ZTF (pluses), ATLAS (squares), and ASAS-SN (pentagons). The ASAS-SN discovery point is denoted with an enlarged pentagonal marker and vertical black line, and the epoch of first light with a dashed black line with the grey area denoting the 3σ uncertainty in the fit that determined the epoch of first light (the one- and two-component power laws have a consistent value of t_0). Short, black lines along the horizontal axis correspond to optical spectral observations, along with a dotted maroon line for our NIR spectral observation. Downward-pointing triangles denote upper limits. All magnitudes are in the AB system and are host subtracted. No correction for the (small) Milky-Way extinction is applied. All points without visible uncertainties have uncertainties smaller than the data markers.

Table 5. MCMC fit results for the light curve rise.

Parameter	One-component value	Two-component value
f_0 [μJy]	-1^{+21}_{-22}	1^{+22}_{-21}
t_0 [MJD]	59988^{+1}_{-1}	59988^{+1}_{-1}
h [μJy]	132^{+95}_{-69}	163^{+141}_{-81}
α/α_1	$1.1^{+0.3}_{-0.3}$	$1.2^{+0.4}_{-0.3}$
α_2		$-0.1^{+0.1}_{-0.1}$

best-fitting values are $a = 4.2 \times 10^{-14}$ erg s^{-1} cm^{-2} Å^{-1}, $b = -0.54$, and $c = -4.5 \times 10^{-16}$ erg s^{-1} cm^{-2} Å^{-1}. However, because the NIR is not host subtracted, there is most likely host contamination, which may influence the fitted power-law slope.

We see prominent H α and weak H δ and He I emission in all our optical spectra, along with He II λ4686 in the earliest spectra. While there is also He II λ3100 emission in the Keck-I LRIS spectrum. The rest of our spectral data do not extend this far into the blue. From these features, ASASSN-23bd is a member of the H + He TDE class (Leloudas et al. 2019; van Velzen et al. 2021). We fit the H α line with a Gaussian using a linear continuum model normalized to the line bracketing regions 6100 Å $\leq\lambda\leq$ 6230 Å and 7600 Å $\leq\lambda\leq$ 7900 Å. Fig. 10 shows the evolution of the H α feature over time, as well as our Gaussian fits. Fig. 11 displays the integrated luminosity of each Gaussian and its FWHM. As the phase increases, the H α luminosity monotonically declines. We find evidence for a correlation between H α integrated luminosity and FWHM with a Kendall τ value of 0.473 corresponding to a p value of 0.001, suggesting a weak linear trend. This is the typical evolution of a TDE, where spectral lines narrow as they become less luminous.

4 DISCUSSION

4.1 TDE or AGN flare?

While ASASSN-23bd was initially classified as a TDE and Zhu et al. (2023) rule out a Type II supernova due to the lack of low-ionization

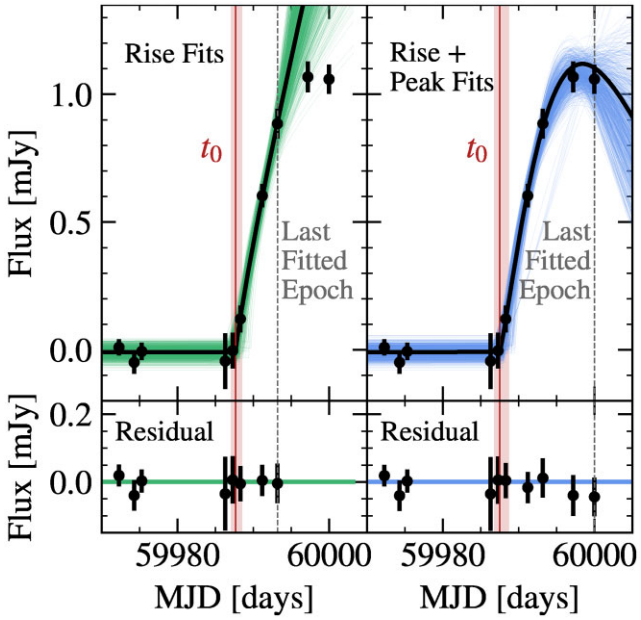

Figure 4. Single (left) and double (right) power-law fits to the rise of ASASSN-23bd. The best fit is shown in black, with individual samples shown in green (left) and blue (right). The bottom panels show the fit residuals. Section 3.2 describes the fit models, and Table 5 presents the fit parameters for both models.

Table 6. MOSFiT results for ASASSN-23bd.

Quantity	Value	Units
$\log R_{\rm ph0}$	$1.2^{+0.6}_{-0.2}$	–
$\log T_{\rm visc}$	$0.7^{+0.2}_{-0.2}$	d
b	$1.0^{+0.1}_{-0.1}$	–
$\log M_h$	$6.4^{+0.1}_{-0.1}$	$M_\odot$
$\log \epsilon$	$-3.2^{+0.7}_{-0.5}$	–
l	$1.2^{+0.3}_{-0.2}$	–
$\log n_{\rm H,\,host}$	$21.3^{+0.1}_{-0.1}$	$\rm cm^{-2}$
$M_\star$	$0.5^{+0.9}_{-0.1}$	$M_\odot$
$t_{\rm exp}$	$-0.3^{+0.2}_{-0.4}$	d
$\log \sigma$	$0.6^{+0.1}_{-0.1}$	–

The middle columns present the lower uncertainty, median value, and upper uncertainty for a 1σ confidence interval. We include only the statistical error in our reported values. For a discussion of systematic errors, see Mockler et al. (2019). $\log R_{\rm ph0}$: photosphere power-law constant; $\log T_{\rm visc}$: viscous delay time scale; b: scaled impact parameter β; $\log M_h$: SMBH mass; $\log \epsilon$: efficiency; l: photosphere power-law exponent; $\log n_{\rm H,\,host}$: local hydrogen column density; $M_\star$: stellar mass; t_{exp}: time of disruption; $\log \sigma$: model variance.

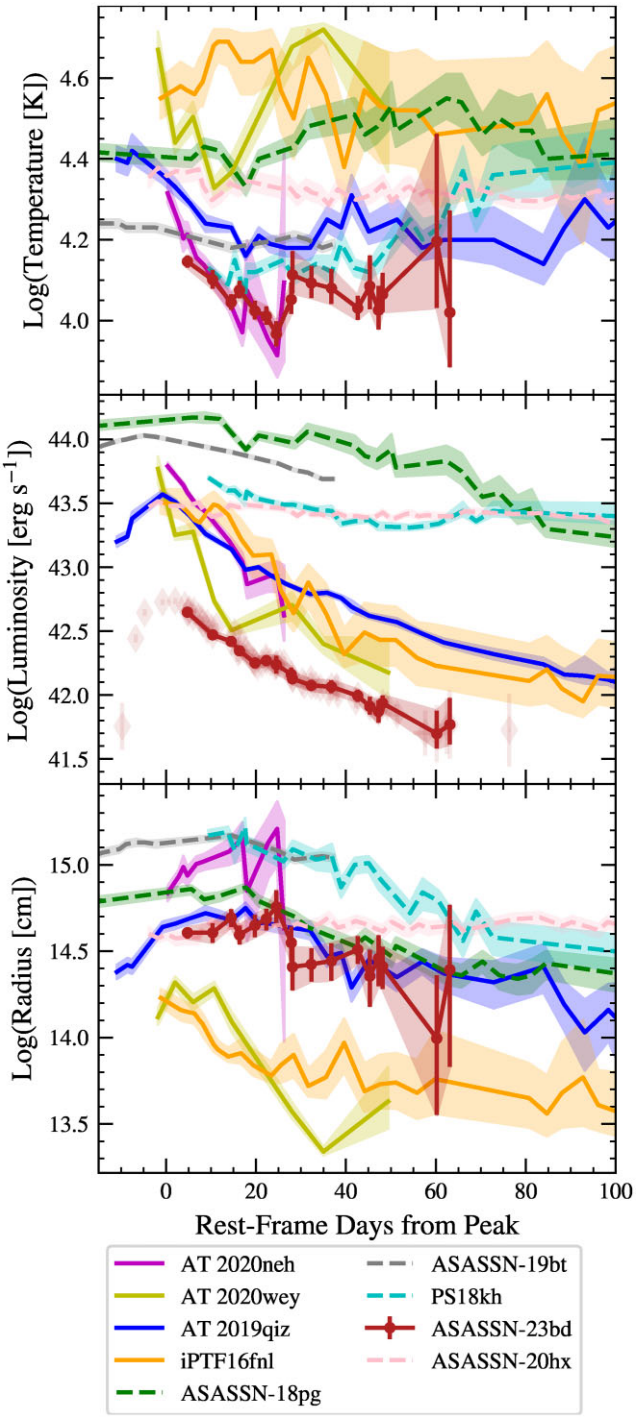

Figure 5. Evolution of the blackbody temperature (top), luminosity (centre), and radius (bottom) of ASASSN-23bd (red with points) and other TDEs (other colours). FaF TDEs are shown as solid lines, whereas other nuclear transients use dashed lines. In the middle panel, the bolometrically corrected ASAS-SN photometry is shown in faint, red diamonds, assuming only a Milky Way extinction and the blackbody fits described in the text. The bolometric luminosity from *Swift* is shown in bold, red circles.

metals in the spectra near peak, the indicators of weak AGN activity in NGC 3799 might imply that ASASSN-23bd could instead be an AGN flare. For example, 'starved', low-luminosity AGNs such as NGC 3799 may have occasional flares that resemble TDEs (Saxton, Perets & Baskin 2018). In this section, we evaluate the observations of ASASSN-23bd to determine if it is indeed a TDE or, instead, an AGN flare from an otherwise quiescent AGN.

We observe a rapid rise to peak and a smooth decline thereafter, a hot constant blackbody temperature, no Mg II or Fe II emission features, and a central SMBH mass less than 10^8 $M_\odot$. These characteristics are generally attributed to TDEs rather than AGN flares (Frederick et al. 2021; Zabludoff et al. 2021). Our NIR spectrum does not show spectral features, unlike the spectra of AGN and CL-AGN (Landt et al. 2008; Neustadt et al. 2023). Furthermore, a LINER designation does not necessarily signify the presence of an AGN. The line ratios seen for LINERs may also originate from post-

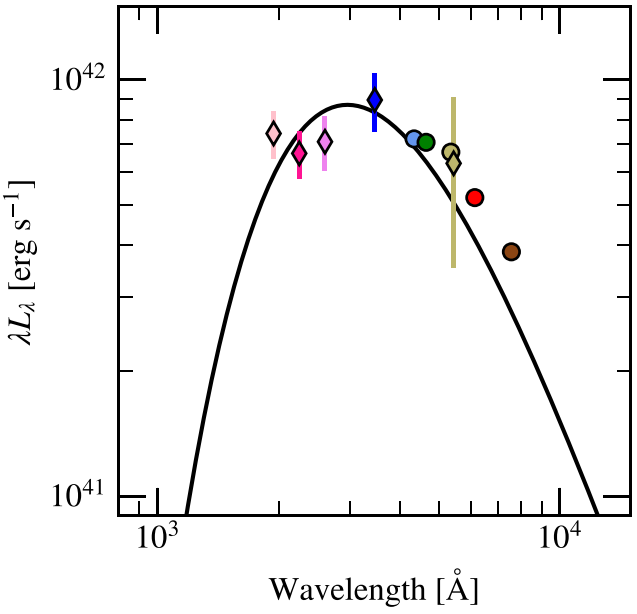

Figure 6. The best-fitting UV/optical blackbody (black line) of ASASSN-23bd at MJD ∼60030. The photometric data have the same markers and colours as Fig. 3.

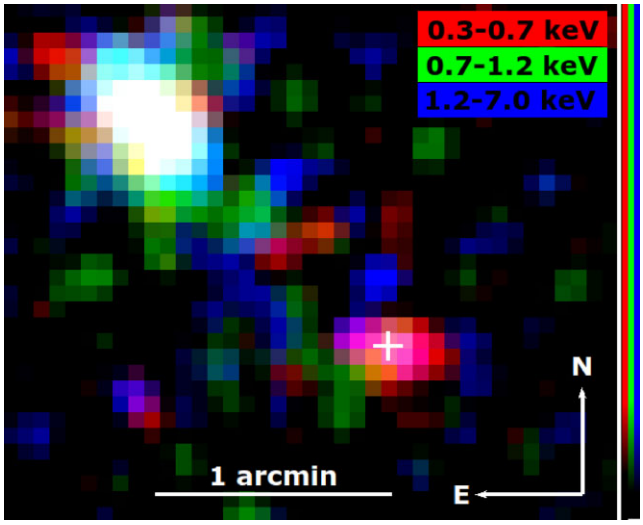

Figure 7. XMM-Newton 3-colour image. The image is smoothed with a 2-pixel Gaussian. The extended emission to the northeast is NGC 3800, the larger, interacting neighbour of NGC 3799. The red, green, and blue colours correspond to 300–700 eV, 700–1200 eV, and 1200–7000 eV, respectively. The white plus sign is the location of ASASSN-23bd.

AGB stars (Yan & Blanton 2012) or merger-induced shocks (Rich, Kewley & Dopita 2015).

The supersoft X-ray spectrum detected by XMM-Newton ∼95 d post-peak also favors the TDE hypothesis. A supersoft spectrum would be unusual for a low-luminosity AGN experiencing stochastic variability (Auchettl et al. 2018). Soft X-ray variability due to a change in obscuration is typically accompanied by strong hard X-ray emission (e.g. Sazonov et al. 2007), which we do not see here. Conversely, an observed soft X-ray spectrum is expected and commonly observed in TDEs (e.g. Auchettl et al. 2017; Auchettl et al. 2018; van Velzen et al. 2021; Guolo et al. 2023). For a TDE, the earliest *Swift* non-detection implies that any earlier X-ray peak must be very weak or that there is only a late-time rise, as has been observed in other TDEs (e.g. ASASSN-15oi Gezari, Cenko & Arcavi 2017; Holoien et al. 2018, OGLE16aaa Kajava et al. 2020, ASASSN-19dj Hinkle et al. 2021b, and eRASSt J074426.3 + 291606 Malyali et al. 2023). While the X-ray data do not conclusively point to a TDE interpretation, a growing number of AGN also show soft X-ray emission (e.g. Boller et al. 2021; Jiang et al. 2022; Sacchi, Risaliti & Miniutti 2023), the combined X-ray, UV, optical, and NIR evidence argues for a TDE interpretation.

4.2 The early-time rises of TDEs and other nuclear transients

There are early-time light curve fits for the TDEs ASASSN-19bt (Holoien et al. 2019b), ASASSN-19dj (Hinkle et al. 2021b), ZTF19abzrhgq/AT 2019qiz (Nicholl et al. 2020), ZTF20acitpfz/AT 2020wey (Charalampopoulos et al. 2023), and ASASSN-22ci/AT 2022dbl (Hinkle et al. 2024, in preparation), all of which are consistent with a rise of $f \propto t^2$. ASASSN-23bd, however, has a nearly linear rise. ASASSN-23bd is not alone in this regard: other nuclear transients such as the repeating partial TDE ASASSN-14ko (Payne et al. 2021; Tucker et al. 2021; Cufari, Coughlin & Nixon 2022; Payne et al. 2022; Liu et al. 2023) and the ANT ASASSN-20hx (Hinkle et al. 2022) also display linear rises.

Interestingly, the majority of TDEs with t^2 rises have hosts that do not display AGN activity, whereas the hosts of the linearly-rising ASASSN-14ko, ASASSN-20hx, and ASASSN-23bd show signs of AGN activity. Thus, AGN activity and early-time light curve rise shape may be connected since TDEs in host galaxies with AGN activity predominantly have $f \propto t$ rises while those in non-AGN hosts exclusively have $f \propto t^2$ rises. There are currently no theoretical explanations for the trends seen in the early-time rises of TDEs, including the now-apparent bimodality between linear and quadratic rises. There are no models for the origin of a $f \propto t$ rise as opposed to a $f \propto t^2$ rise, which can be caused by a constant expansion velocity at a fixed photospheric temperature. Further early-time observations of TDEs are needed to determine if there is a correlation.

4.3 Comparison to other low-redshift nuclear transients

While ASASSN-23bd is the lowest-luminosity optically selected TDE to date, several other nuclear transients at low redshift have been claimed as TDEs. Many of these sources have lower UV/optical luminosities than ASASSN-23bd, either because they are intrinsically fainter at these wavelengths or are more heavily obscured than a typical TDE.

First, Malyali et al. (2023) present the 'low luminosity and slow' TDE eRASSt J074426.3 + 291606 (J0744), an X-ray-selected TDE that has a low intrinsic ultraviolet/optical luminosity. Given the significant X-ray emission, it is unsurprising that J0744 has a greater bolometric luminosity than ASASSN-23bd. Unlike FaF TDEs, J0744 declines slowly. This may be explained by either photon trapping within an outflow (Metzger & Stone 2016) or low circularization efficiency (Steinberg & Stone 2022)). One prediction of circularization efficiency variations is delayed soft X-ray emission in FaF TDEs, so future X-ray follow-up of ASASSN-23bd will help validate the mechanism differentiating between 'low luminosity and slow' and FaF TDEs.

Secondly, Panagiotou et al. (2023) claim WTP14adbjsh, a heavily-obscured nuclear flare discovered in the IR at $z = 0.0106$, is a TDE, but there is no definitive evidence for a TDE interpretation. Similar to ASASSN-23bd, the pre-flare WISE $W1 - W2$ colour of the host

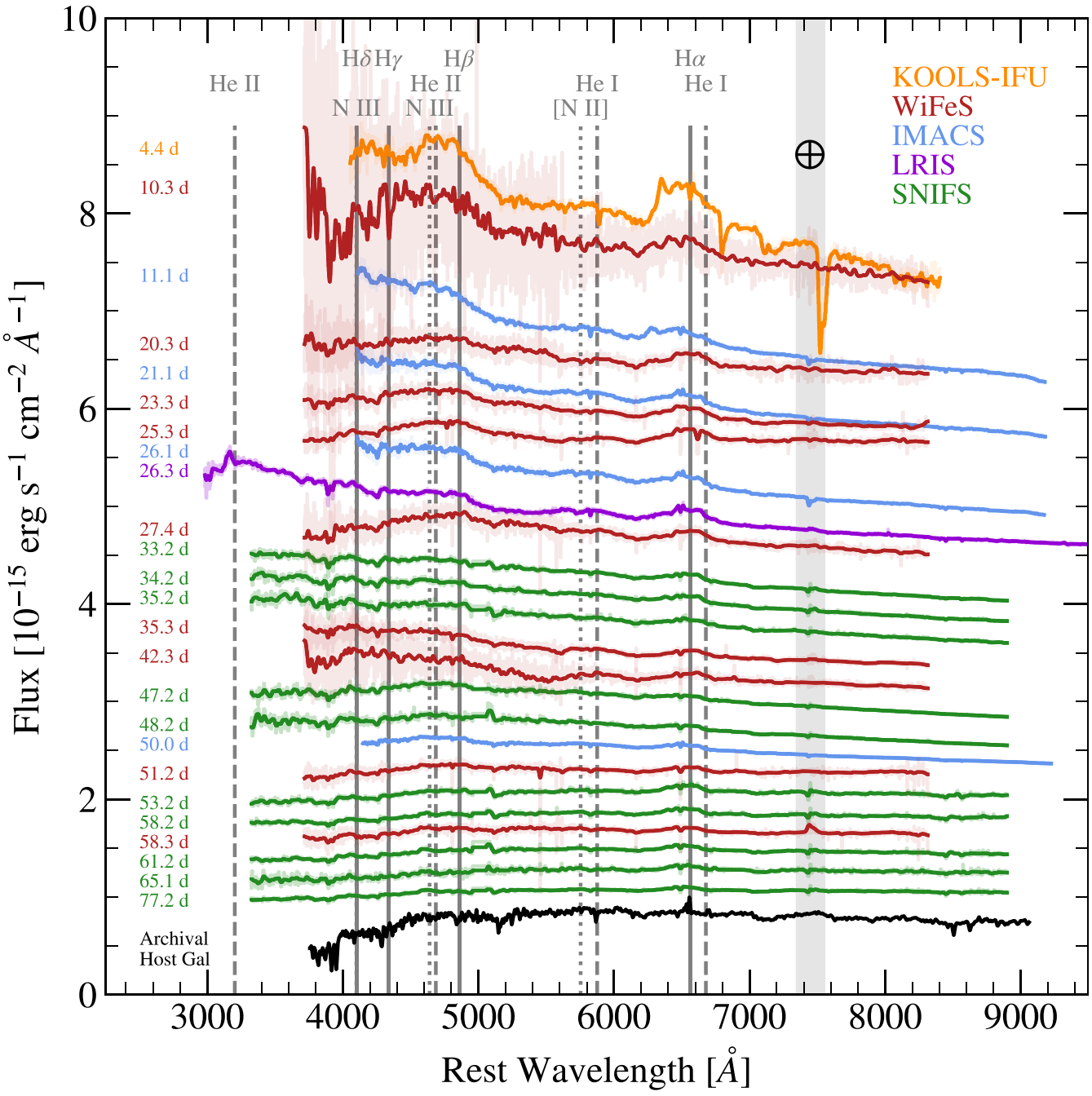

Figure 8. Optical spectra of ASASSN-23bd corrected to match the observed Swope *g*, *r*, and *i* photometry. Common H, He, and N lines are marked by solid, dashed, and dotted grey lines, respectively. The fainter lines are the original spectra, and the bold lines are smoothed spectra. Our spectra range from +4.4 d (top) after discovery to +77.2 d (bottom) after discovery. Spectra are from the KOOLS-IFU (orange), WiFeS (red), IMACS (blue), SNIFS (green), and LRIS (purple). The archival SDSS spectrum is in black. We do not have access to the original KOOLS-IFU data, so we cannot improve the data reduction. Besides the telluric feature, which is redder than the rest of our spectra, the wavelengths align with the rest of our data.

cannot rule out weak AGN activity, nor does its location on galaxy diagnostic diagrams (e.g. the WHAN diagram) exclude LINER-like or weak AGN behaviour. While optical surveys do not find previous AGN variability, the large extinction ($A_V \approx 9$ mag based on their Na I D EW measurements and the relationship in Poznanski et al. 2012) prevents robust constraints on AGN activity from archival survey data, leaving the TDE interpretation uncertain.

Thirdly, Nikołajuk & Walter (2013) and Irwin et al. (2015) present observations of IGR J12580+0134, a claimed X-ray-selected TDE. While the host of IGR J12580 + 0134 has shown AGN activity and is a known Seyfert 2 galaxy, Nikołajuk & Walter (2013) argue for a TDE interpretation based on the extreme hard and soft band X-ray brightness. Hosted in NGC 4845 with a redshift of 0.003663 (Springob et al. 2005), this would be the lowest-redshift TDE to date.

Finally, from the arguments presented in this work, we believe that ASASSN-23bd is the strongest of these nearby TDE candidates based on the comprehensive X-ray, UV, optical, and NIR follow-up observations in this work and a radio detection (Sfaradi et al. 2023). Interestingly, each low-redshift TDE candidate has some evidence for potential AGN activity, including ASASSN-23bd (although we

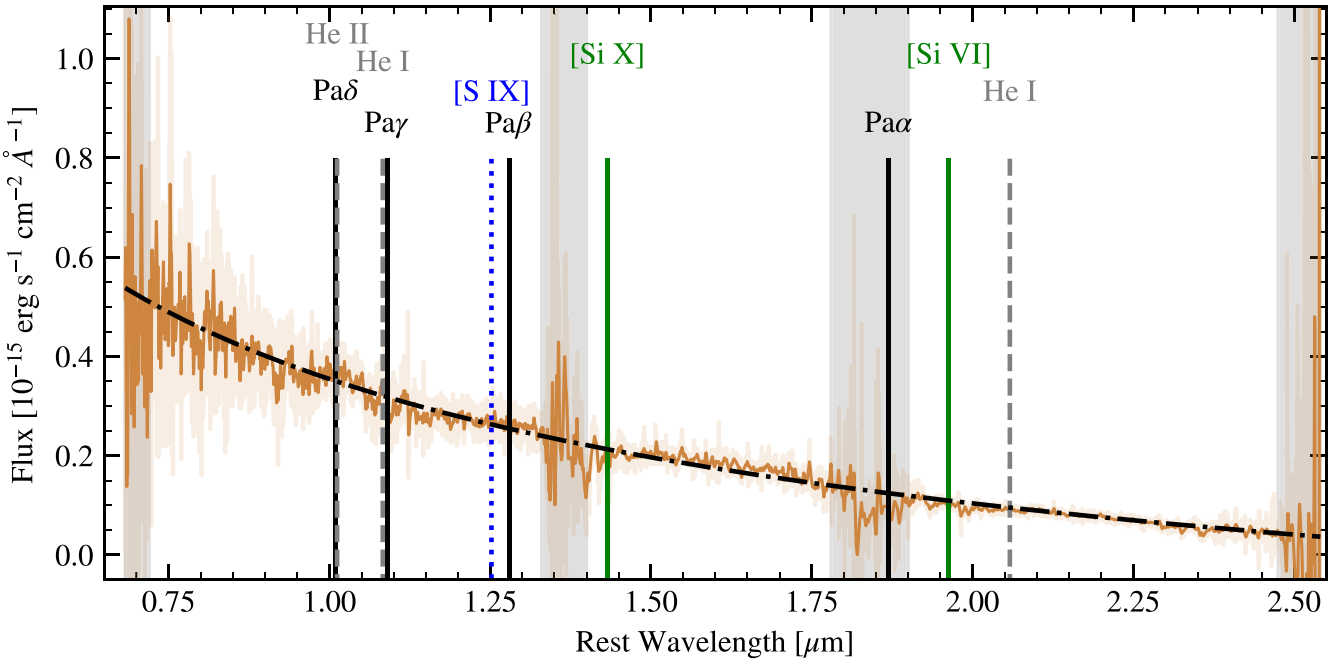

Figure 9. Rest-frame NIR spectrum of ASASSN-23bd. No AGN features, such as H, He, or coronal emission lines, are visible in the spectrum. Solid grey lines are Paschen series H lines; the dashed grey line is He ɪλ 1.083. Coronal S and Si lines are denoted with dotted blue and solid green lines, respectively. The middle two grey regions denote regions contaminated by telluric absorption. The shaded grey areas are data excluded from the fit; the dash–dotted black line is the best power-law fit.

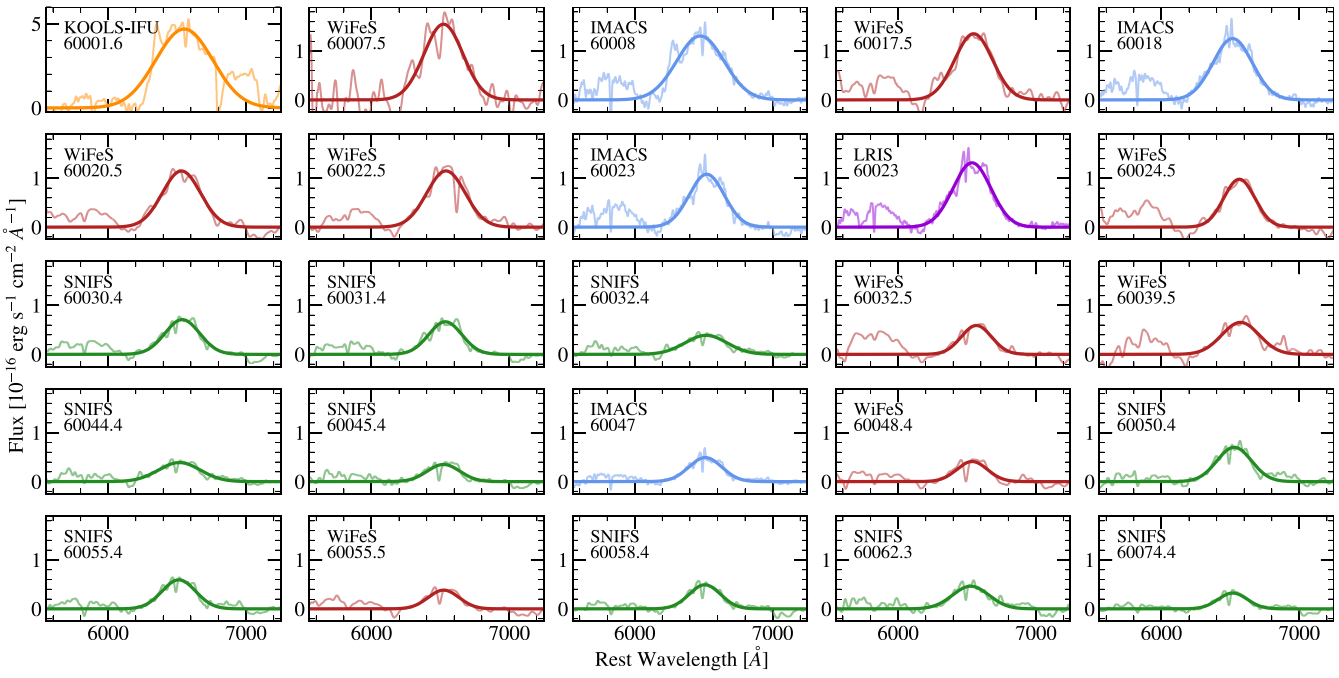

Figure 10. H α emission features and their fitted Gaussian profiles. The colour scheme is the same as in Fig. 8. The spectra were continuum subtracted using a linear fit to each spectrum between 6100 Å $\leq\lambda\leq$ 6230 Å and 7600 Å $\leq\lambda\leq$ 7900 Å. A smoothing function is applied to the plotted spectra.

rule out an AGN interpretation in Section 4.1). Regardless of the classification for each object, further monitoring for delayed features such as soft X-ray emission or coronal lines like those recently detected in the FaF TDE AT 2019qiz (Short et al. 2023), may improve our understanding of the long-term ramifications of accretion-powered flares on SMBHs.

4.4 Comparison to other TDEs

In this subsection, we compare ASASSN-23bd to other TDEs and nuclear transients. Our comparison sample consists of iPTF16fnl (Blagorodnova et al. 2017), PS18kh (van Velzen et al. 2019a; Holoien et al. 2019b), ASASSN-18pg (Holoien et al. 2018), ASASSN-19bt

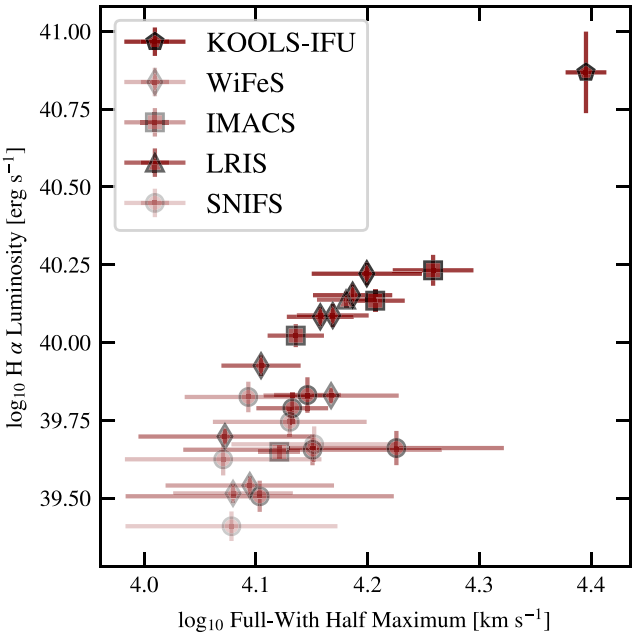

Figure 11. The H α luminosities and FWHM of ASASSN-23bd. There is a weak linear trend between the width and luminosity of the feature, with wider features generally being more luminous. Each point is shaded based on epoch, with earlier epochs being darker and later epochs being lighter. Different symbols are used based on the instrument used to acquire the data.

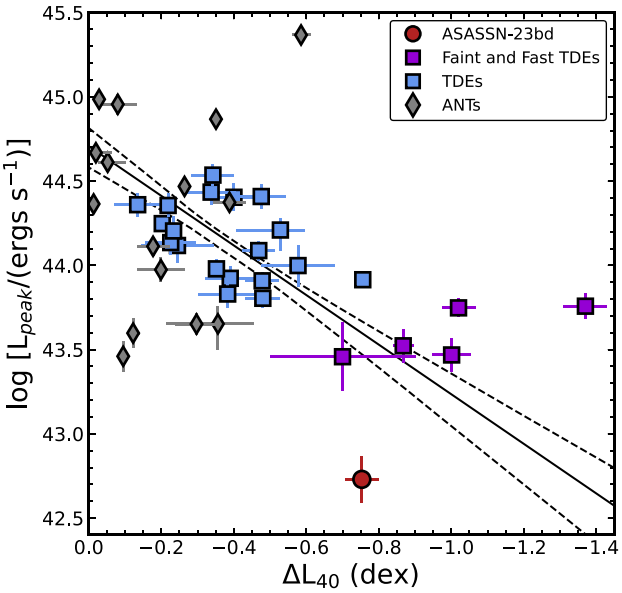

Figure 12. The peak-decline relationship for TDEs (Hinkle et al. 2020). ASASSN-23bd is the red circle, other FaF TDEs are the purple squares, and other slower TDEs are the blue squares. ASASSN-23bd has the lowest luminosity of our entire comparison sample. The decline of ASASSN-23bd is faster than almost all of the normal TDE in our comparison sample, but it is relatively slow compared to the other FaF TDEs.

(Holoien et al. 2019c), AT 2019qiz (Nicholl et al. 2020), AT 2020neh (Angus et al. 2022), ASASSN-20hx (Hinkle et al. 2022), and AT 2020wey (Charalampopoulos et al. 2023). We compiled this sample by selecting FaF TDEs and several 'normal' TDEs observed at peak. We also include the ANT ASASSN-20hx since it also has a linearly rising early-time light curve. The data are taken from the literature except for AT 2020neh and AT 2020wey, which we re-fit using the *Swift* photometry from Angus et al. (2022) and Charalampopoulos et al. (2023), respectively.

In Fig. 5, ASASSN-23bd has the lowest temperature and luminosity in our sample. While the temperature of ASASSN-23bd is similar to AT 2020neh and PS18kh, it is cooler than the other FaF TDEs. In addition to being the least luminous object in our sample, ASASSN-23bd also rapidly declines in luminosity with a decline rate similar to iPTF16fnl, AT 2019qiz, and AT 2020wey but not quite as steep as AT 2020neh. The Eddington luminosity derived for the $M_{\rm BH}$ estimate from Section 3.1 is 2.0×10^{44} erg s^{-1}. The peak bolometric luminosity of ASASSN-23bd is $(5.4 \pm 0.4) \times 10^{42}$ erg s^{-1}, corresponding to an Eddington ratio of $L_{\rm peak}/L_{\rm Edd} = 2.7 \times 10^{-2}$. This is smaller than every TDE analysed by Mockler et al. (2019), where the smallest Eddington ratio was 0.11, and two orders of magnitude smaller than the typical value of $\sim$1 found by Wevers et al. (2019). ASASSN-23bd is the least optical/UV luminous TDE in the sample. Finally, the blackbody radius of ASASSN-23bd is similar to ASASSN-18pg, AT 2019qiz, and AT 2020neh and larger than AT 2020wey and iPTF16fnl. This may be an empirical indicator for TDEs occurring in AGN hosts since ASASSN-23bd and AT 2019qiz are also in weak AGN galaxies, but the sample size is still small.

Fig.12 shows the peak-decline relationship for TDEs (Hinkle et al. 2020) along with the ANTs for comparison. ASASSN-23bd is less luminous than the rest of our sample, with a peak luminosity of $\sim 10^{42.7}$ erg s^{-1}, whereas the 'normal' TDE sample clusters between $\sim 10^{44.0}$ to $\sim 10^{44.5}$ erg s^{-1}. The decline parameter ΔL_{40} is defined as

$$\Delta L_{40} \equiv \log_{10}\left(\frac{L_{40}}{L_{\rm peak}}\right). \quad (4)$$

ASASSN-23bd has a decline parameter of $\Delta L_{40} \approx -0.7$ dex, which is faster than the normal TDEs with $\Delta L_{40} \sim -0.2$ dex to ~ -0.6 dex, and the ANTs which have $\Delta L_{40} \sim 0.0$ dex to ~ -0.4 dex. However, this is a slower decline than most of the other FaF TDEs.

ASASSN-23bd shows several spectral similarities to the FaF TDEs iPTF16fnl (Blagorodnova et al. 2017), ATLAS18mlw (Hinkle et al. 2023), AT 2019qiz (Nicholl et al. w), AT 2020neh (Angus et al. 2022), and AT 2020wey (Charalampopoulos et al. 2023). We show the spectra closest to maximum light for each of these TDEs in Fig. 13. Both iPTF16fnl and AT 2020wey show H α and He I emission, whereas AT 2020neh shows only H α. ASASSN-23bd also shows prominent H α emission while its He I emission is weaker than iPTF16fnl and AT 2020wey. Prior to peak, all three of these other TDEs show strong He II emission, which quickly fades post-peak. The He II line is present in our WiFes and IMACS spectra at +4 d and +5 d, respectively, and in the LRIS spectrum at +26.3 d.

Since there are limited UV spectra of TDEs, we assemble a separate comparison sample of objects with HST spectroscopy. The comparison objects are ASASSN-14li (Cenko et al. 2016), iPTF15af (Blagorodnova et al. 2019), iPTF16fnl (Brown et al. 2018), PS18kh (Hung et al. 2019), ZTF19abzrhg/AT 2019qiz (Hung et al. 2021), and the composite SDSS QSO spectrum from Vanden Berk et al. (2001). These TDEs and ASASSN-23bd are shown in Fig. 14. Compared to the other TDEs with UV spectra, ASASSN-23bd is most similar to iPTF15af (Blagorodnova et al. 2019) and iPTF16fnl (Brown et al. 2018). While those two objects have various emission features blueward of $\sim$1800 Å and noticeable blackbody continua, the spectrum of ASASSN-23bd is much cooler and does not exhibit carbon or Lyman α emission lines. Conversely, all three TDEs exhibit

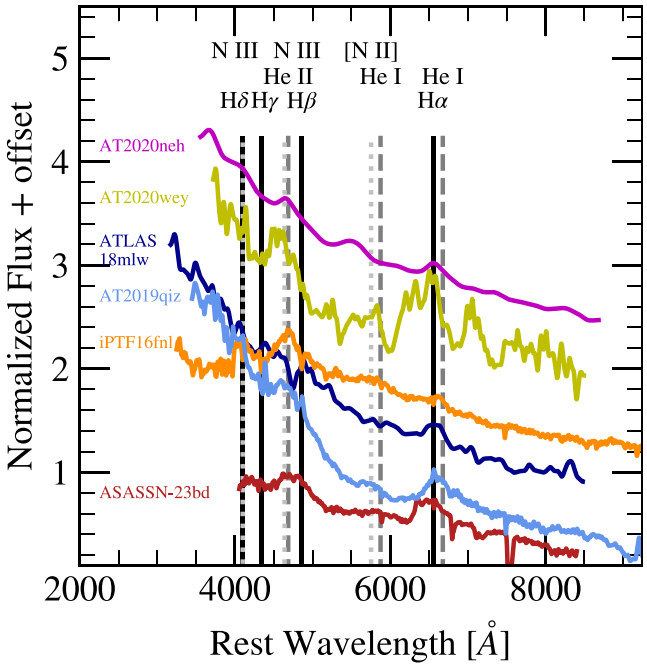

Figure 13. Maximum light spectra of FaF TDEs. The flux is normalized to the median value of the entire spectrum and offset by a constant. The solid, black lines indicate H features, the dashed, grey lines indicate He features, and the dotted, grey lines indicate N features.

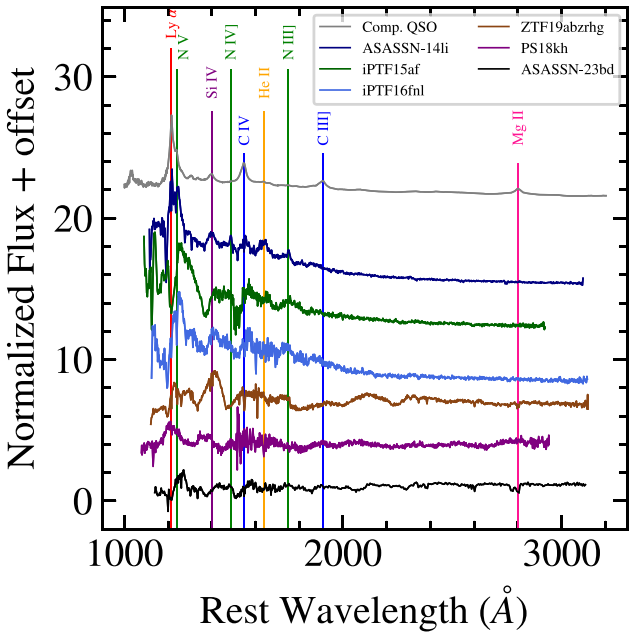

Figure 14. Rest-frame UV spectrum of ASASSN-23bd and other TDEs and an SDSS composite QSO spectrum from (Vanden Berk et al. 2001). The comparison TDEs are ASASSN-14li (Cenko et al. 2016), iPTF15af (Blagorodnova et al. 2019), iPTF16fnl (Brown et al. 2018), PS18kh (van Velzen et al. 2019a; Holoien et al. 2019b), and ZTF19abzrhg/AT 2019qiz (Hung et al. 2019). The TDE spectra have been binned to ∼1.5Å, normalized by their median UV flux, and offset by a constant for visibility. The phase in the caption is relative to peak, or discovery for sources not observed before the peak. Several lines commonly seen in the UV spectra of TDEs or AGNs are marked.

nitrogen emission features such as N III] and N IV]. This is consistent with the claim that TDEs can be enriched in nitrogen, whereas AGNs should have carbon and Mg II emission instead (Kochanek 2016; Mockler et al. 2022). Mg II appears to be a good diagnostic to differentiate between TDEs and AGNs. No TDE to date has exhibited Mg II emission.

5 SUMMARY

We present the discovery and multiband photometric and spectroscopic data of the FaF nuclear transient ASASSN-23bd in NGC 3799. NGC 3799 is a star-forming galaxy with signs of potential weak AGN activity. ASASSN-23bd peaked on MJD $60\,000^{+3}_{-3}$, had a peak UV/optical luminosity of $(5.4 \pm 0.4) \times 10^{42}$ erg s^{-1}, and has a near peak X-ray upper limit of 1.75×10^{40} erg s^{-1} and late-time X-ray detection of $L_{0.3-2\mathrm{keV}} = 4.2 \times 10^{39}$ erg s^{-1}. Spectroscopically, ASASSN-23bd shows $H\alpha$ emission throughout its decline, as well as He II emission near peak and He I emission shortly after the peak. The early rise of ASASSN-23bd is well fit by a near linear power law ($f \propto t^a$ with an exponent $a = 1.1 \pm 0.3$). We speculate that TDEs in galaxies with no AGN activity seem to rise with $f \propto t^2$ power laws, whereas TDEs in galaxies with existing AGN activity seem to prefer $f \propto t$ rises.

The UV/optical SED of ASASSN-23bd is well fit by a blackbody, and the blackbody temperature is among the coolest of all FaF TDEs with values and evolution most similar to AT 2020neh. The luminosity is less than any other FaF TDE such as iPTF16fnl, AT 2020wey, and AT 2020neh.

ASASSN-23bd is the lowest redshift TDE to date and due to its low luminosity, ASASSN-23bd may not have been detected if it were not so close to us. In this sense, ASASSN-23bd is a fine but fortunate addition to the collection of FaF TDEs. More FaF TDEs should be discovered by deeper sky surveys such as LSST, providing further advances in the understanding of the variety of nuclear transients.

ACKNOWLEDGEMENTS

We thank the referee for providing helpful comments that improved this manuscript. We thank Erin Kara and Adam Malyali for their helpful comments on the manuscript. We thank Las Cumbres Observatory and its staff for their continued support of ASAS-SN. ASAS-SN is funded in part by the Gordon and Betty Moore Foundation through grants GBMF5490 and GBMF10501 to the Ohio State University and also funded in part by the Alfred P. Sloan Foundation grant G-2021-14192.

This material is based upon work supported by the National Science Foundation Graduate Research Fellowship Program under Grant No. 2236415. Any opinions, findings, and conclusions or recommendations expressed in this material are those of the author(s) and do not necessarily reflect the views of the National Science Foundation.

KA would also like to acknowledge Ian Price and Chris Lidman with the ANU 2.3-m telescope. The automation of the ANU 2.3-m telescope was made possible through funding provided by the Centre of Gravitational Astrophysics at the Australian National University.

CSK and KZS are supported by National Science Foundation grants AST-1907570 and 2307385.

MDS is funded by the Independent Research Fund Denmark (IRFD, grant number 10.46540/2032-00022B)

LG acknowledges financial support from the Spanish Ministerio de Ciencia e Innovación (MCIN) and the Agencia Estatal de

Investigación (AEI) 10.13039/501100011033 under the PID2020-115253GA-I00 HOSTFLOWS project, from Centro Superior de Investigaciones Científicas (CSIC) under the PIE project 20215AT016 and the program Unidad de Excelencia María de Maeztu CEX2020-001058-M, and from the Departament de Recerca i Universitats de la Generalitat de Catalunya through the 2021-SGR-01270 grant.

JL acknowledges support from National Science Foundation grant AAG-2206523.

This research is based on observations made with the NASA/ESA Hubble Space Telescope obtained from the Space Telescope Science Institute, which is operated by the Association of Universities for Research in Astronomy, Inc., under NASA contract NAS 5–26555. These observations are associated with program(s) GO 17001. Based on observations obtained with XMM-Newton, an ESA science mission with instruments and contributions directly funded by ESA Member States and NASA.

Based on observations gathered at the 6.5-m Magellan I (Baade) telescope and the 1-m Swope telescope at Las Campanas Observatory (Chile).

WBH is an NSF Fellow. MAT is a CCAPP Fellow.

DATA AVAILABILITY

Data is available upon reasonable request to the corresponding author. Spectra will be uploaded to WISeREP upon publication.

REFERENCES

Aguado D. S. et al., 2019, ApJS, 240, 23
Alard C., 2000, AAPS, 144, 363
Alard C., Lupton R. H., 1998, ApJ, 503, 325
Albareti F. D. et al., 2017, ApJS, 233, 25
Angus C. R. et al., 2022, Nat. Astron., 6, 1452
Arcavi I. et al., 2014, ApJ, 793, 38
Auchettl K., Guillochon J., Ramirez-Ruiz E., 2017, ApJ, 838, 149
Auchettl K., Ramirez-Ruiz E., Guillochon J., 2018, ApJ, 852, 37
Bade N., Komossa S., Dahlem M., 1996, A&A, 309, L35
Baldwin J. A., Phillips M. M., Terlevich R., 1981, PASP, 93, 5
Bellm E. C. et al., 2019, PASP, 131, 018002
Biehl D., Boncioli D., Lunardini C., Winter W., 2018, Sci. Rep., 8, 10828
Blagorodnova N. et al., 2017, ApJ, 844, 46
Blagorodnova N. et al., 2019, ApJ, 873, 92
Bloom J. S. et al., 2011, Science, 333, 203
Boller T. et al., 2021, A&A, 647, A6
Brassart M., Luminet J. P., 2008, A&A, 481, 259
Breeveld A. A., Landsman W., Holland S. T., Roming P., Kuin N. P. M., Page M. J., 2011, in McEnery J. E., Racusin J. L., Gehrels N.eds, American Institute of Physics Conference Series. Vol. 1358, Gamma Ray Bursts 2010. p. 373, preprint (arXiv:1102.4717)
Brinchmann J., Charlot S., White S. D. M., Tremonti C., Kauffmann G., Heckman T., Brinkmann J., 2004, MNRAS, 351, 1151
Brown P. J., Breeveld A. A., Holland S., Kuin P., Pritchard T., 2014, Ap&SS, 354, 89
Brown J. S., Shappee B. J., Holoien T. W.-S., Stanek K. Z., Kochanek C. S., Prieto J. L., 2016, MNRAS, 462, 3993
Brown J. S., Holoien T. W.-S., Auchettl K., Stanek K. Z., Kochanek C. S., Shappee B. J., Prieto J. L., Grupe D., 2017, MNRAS, 466, 4904
Brown J. S. et al., 2018, MNRAS, 473, 1130
Bruzual G., Charlot S., 2003, MNRAS, 344, 1000
Burns C. R. et al., 2018, ApJ, 869, 56
Burns C. et al., 2021, Astron. Telegram, 14441, 1
Burrows D. N. et al., 2005, SSR, 120, 165
Burrows D. N. et al., 2011, Nature, 476, 421
Carter B., Luminet J. P., 1983, A&A, 121, 97
Cenko S. B. et al., 2012a, MNRAS, 420, 2684
Cenko S. B. et al., 2012b, ApJ, 753, 77
Cenko S. B. et al., 2016, ApJ, 818, L32
Chambers K. C. et al., 2016, preprint (arXiv:1612.05560)
Chan C.-H., Piran T., Krolik J. H., Saban D., 2019, ApJ, 881, 113
Charalampopoulos P., Pursiainen M., Leloudas G., Arcavi I., Newsome M., Schulze S., Burke J., Nicholl M., 2023, A&A, 673, A95
Charalampopoulos P. et al., 2024, preprint (arXiv:2401.11773)
Childress M. J., Vogt F. P. A., Nielsen J., Sharp R. G., 2014, Ap&SS, 349, 617
Chornock R. et al., 2014, ApJ, 780, 44
Cid Fernandes R., Stasińska G., Mateus A., Vale Asari N., 2011, MNRAS, 413, 1687
Coughlin E. R., Nixon C. J., 2019, ApJ, 883, L17
Cufari M., Coughlin E. R., Nixon C. J., 2022, ApJ, 929, L20
Cushing M. C., Vacca W. D., Rayner J. T., 2004, PASP, 116, 362
Dai L., McKinney J. C., Miller M. C., 2015, ApJ, 812, L39
Dai L., McKinney J. C., Roth N., Ramirez-Ruiz E., Miller M. C., 2018, ApJ, 859, L20
de Vaucouleurs G., de Vaucouleurs A., Corwin Herold G. J., Buta R. J., Paturel G., Fouque P., 1991, Third Reference Catalogue of Bright Galaxies. Springer
Domínguez A. et al., 2013, ApJ, 763, 145
Dopita M., Hart J., McGregor P., Oates P., Bloxham G., Jones D., 2007, Ap&SS, 310, 255
Dopita M. et al., 2010, Ap&SS, 327, 245
Dressler A., Hare T., Bigelow B. C., Osip D. J., 2006, in McLean I. S., Iye M.eds, Proc. SPIE Conf. Ser., Vol. 6269, Ground-based and Airborne Instrumentation for Astronomy. SPIE, Bellingham. p. 62690F
Eisenstein D. J. et al., 2011, AJ, 142, 72
Evans C. R., Kochanek C. S., 1989, ApJ, 346, L13
Farrar G. R., Piran T., 2014, preprint (arXiv:1411.0704)
Fausnaugh M. M. et al., 2021, ApJ, 908, 51
Folatelli G. et al., 2013, ApJ, 773, 53
Foreman-Mackey D., Hogg D. W., Lang D., Goodman J., 2013, PASP, 125, 306
Frederick S. et al., 2021, ApJ, 920, 56
French K. D., Arcavi I., Zabludoff A., 2016, ApJ, 818, L21
Gafton E., Rosswog S., 2019, MNRAS, 487, 4790
Galbany L. et al., 2023, A&A, 679, A95
Gallegos-Garcia M., Law-Smith J., Ramirez-Ruiz E., 2018, ApJ, 857, 109
Gaskell C. M., Rojas Lobos P. A., 2014, MNRAS, 438, L36
Gehrels N. et al., 2004, ApJ, 611, 1005
Gezari S. et al., 2006, ApJ, 653, L25
Gezari S. et al., 2008, ApJ, 676, 944
Gezari S. et al., 2009, ApJ, 698, 1367
Gezari S. et al., 2012, Nature, 485, 217
Gezari S., Cenko S. B., Arcavi I., 2017, ApJ, 851, L47
Golightly E. C. A., Coughlin E. R., Nixon C. J., 2019, ApJ, 872, 163
Graham A. W., Erwin P., Caon N., Trujillo I., 2001, ApJ, 563, L11
Grupe D., Thomas H.-C., Leighly K. M., 1999, A&A, 350, L31
Guillochon J., Ramirez-Ruiz E., 2013, ApJ, 767, 25
Guillochon J., Ramirez-Ruiz E., 2015, ApJ, 809, 166
Guillochon J., Manukian H., Ramirez-Ruiz E., 2014, ApJ, 783, 23
Guillochon J., Parrent J., Kelley L. Z., Margutti R., 2017, ApJ, 835, 64
Guolo M., Gezari S., Yao Y., van Velzen S., Hammerstein E., Cenko S. B., Tokayer Y. M., 2023, preprint (arXiv:2308.13019)
HI4PI Collaboration, 2016, A&A, 594, A116
Hammerstein E. et al., 2021, ApJ, 908, L20
Hammerstein E. et al., 2023, ApJ, 942, 9
Hamuy M. et al., 2006, PASP, 118, 2
Hart K. et al., 2023, preprint (arXiv:2304.03791)
Henden A. A., Levine S., Terrell D., Welch D. L., 2015, in American Astronomical Society Meeting Abstracts #225. p. 336.16
Hinkle J. T., Holoien T. W. S., Shappee B. J., Auchettl K., Kochanek C. S., Stanek K. Z., Payne A. V., Thompson T. A., 2020, ApJ, 894, L10
Hinkle J. T. et al., 2022, ApJ, 930, 12
Hinkle J. T. et al., 2021b, MNRAS, 500, 1673

Hinkle J. T., Holoien T. W. S., Shappee B. J., Auchettl K., 2021c, ApJ, 910, 83
Hinkle J. T. et al., 2022, ApJ, 930, 12
Hinkle J. T. et al., 2023, MNRAS, 519, 2035
Holoien T. W.-S. et al., 2014a, MNRAS, 445, 3263
Holoien T. W.-S. et al., 2014b, ApJ, 785, L35
Holoien T. W.-S. et al., 2016a, AcA, 66, 219
Holoien T. W.-S. et al., 2016b, MNRAS, 463, 3813
Holoien T. W.-S., Brown J. S., Auchettl K., Kochanek C. S., Prieto J. L., Shappee B. J., Van Saders J., 2018, MNRAS, 480, 5689
Holoien T. W.-S. et al., 2019a, MNRAS, 484, 1899
Holoien T. W. S. et al., 2019b, ApJ, 880, 120
Holoien T. W. S. et al., 2019c, ApJ, 883, 111
Holoien T. W. S. et al., 2020, ApJ, 898, 161
Holoien T. W. S. et al., 2022, ApJ, 933, 196
Hsiao E. Y., Conley A., Howell D. A., Sullivan M., Pritchet C. J., Carlberg R. G., Nugent P. E., Phillips M. M., 2007, ApJ, 663, 1187
Hung T. et al., 2017, ApJ, 842, 29
Hung T. et al., 2019, APJ, 879, 119
Hung T. et al., 2020, ApJ, 903, 31
Hung T. et al., 2021, ApJ, 917, 9
Irwin J. A., Henriksen R. N., Krause M., Wang Q. D., Wiegert T., Murphy E. J., Heald G., Perlman E., 2015, ApJ, 809, 172
Jiang N., Wang T., Hu X., Sun L., Dou L., Xiao L., 2021, ApJ, 911, 31
Jiang J., Gallo L. C., Fabian A. C., Parker M. L., Reynolds C. S., 2022, preprint (arXiv:2205.08236)
Johansson J., Meynardie W., Chu M., Fremling C., 2023, Transient Name Server Classification Report, 2023, 1
Jones D. O. et al., 2021, ApJ, 908, 143
Kajava J. J. E., Giustini M., Saxton R. D., Miniutti G., 2020, A&A, 639, A100
Kara E., Dai L., Reynolds C. S., Kallman T., 2018, MNRAS, 474, 3593
Kewley L. J., Dopita M. A., Sutherland R. S., Heisler C. A., Trevena J., 2001, ApJ, 556, 121
Kewley L. J., Groves B., Kauffmann G., Heckman T., 2006, MNRAS, 372, 961
Kochanek C. S., 1994, ApJ, 422, 508
Kochanek C. S., 2016, MNRAS, 458, 127
Kochanek C. S. et al., 2017, PASP, 129, 104502
Komossa S., 2015, J. High Energy Astrophys., 7, 148
Komossa S., Greiner J., 1999, A&A, 349, L45
Kriek M., van Dokkum P. G., Labbé I., Franx M., Illingworth G. D., Marchesini D., Quadri R. F., 2009, ApJ, 700, 221
Krisciunas K. et al., 2017, AJ, 154, 211
Landolt A. U., 2007, AJ, 133, 2502
Landt H., Bentz M. C., Ward M. J., Elvis M., Peterson B. M., Korista K. T., Karovska M., 2008, ApJS, 174, 282
Lantz B. et al., 2004, in Mazuray L., Rogers P. J., Wartmann R.eds, Proc. SPIE, Vol. 5249, Optical Design and Engineering. SPIE, Bellingham, p. 146,
Law-Smith J., Guillochon J., Ramirez-Ruiz E., 2019, ApJ, 882, L25
Law-Smith J. A. P., Coulter D. A., Guillochon J., Mockler B., Ramirez-Ruiz E., 2020, ApJ, 905, 141
Leloudas G. et al., 2019, APJ, 887, 218
Li R., Ho L. C., Ricci C., Trakhtenbrot B., Arcavi I., Kara E., Hiramatsu D., 2022, ApJ, 933, 70
Liu C., Mockler B., Ramirez-Ruiz E., Yarza R., Law-Smith J. A. P., Naoz S., Melchor D., Rose S., 2023, ApJ, 944, 184
Lodato G., Rossi E. M., 2011, MNRAS, 410, 359
Lodato G., King A. R., Pringle J. E., 2009, MNRAS, 392, 332
Malyali A. et al., 2021, A&A, 647, A9
Malyali A. et al., 2023, MNRAS, 520, 3549
Matsubayashi K. et al., 2019, PASJ, 71, 102
Metzger B. D., Stone N. C., 2016, MNRAS, 461, 948
Mockler B., Guillochon J., Ramirez-Ruiz E., 2019, ApJ, 872, 151
Mockler B., Twum A. A., Auchettl K., Dodd S., French K. D., Law-Smith J. A. P., Ramirez-Ruiz E., 2022, ApJ, 924, 70
Mummery A., 2021, MNRAS, 507, L24
Mummery A., Wevers T., Saxton R., Pasham D., 2023, MNRAS, 519, 5828
Neustadt J. M. M. et al., 2020, MNRAS, 494, 2538
Neustadt J. M. M. et al., 2023, MNRAS, 521, 3810
Nicholl M., 2018, Res. Notes Am. Astron. Soc., 2, 230
Nicholl M. et al., 2020, MNRAS, 499, 482
Nicholl M., Lanning D., Ramsden P., Mockler B., Lawrence A., Short P., Ridley E. J., 2022, MNRAS, 515, 5604
Nikołajuk M., Walter R., 2013, A&A, 552, A75
Oke J. B. et al., 1995, PASP, 107, 375
Panagiotou C. et al., 2023, ApJ, 948, L5
Pasham D. R. et al., 2015, ApJ, 805, 68
Payne A. V. et al., 2021, ApJ, 910, 125
Payne A. V. et al., 2022, ApJ, 926, 142
Phillips M. M., 1993, ApJ, 413, L105
Phillips M. M. et al., 2019, PASP, 131, 014001
Phinney E. S., 1989, Nature, 340, 595
Poole T. S. et al., 2008, MNRAS, 383, 627
Poznanski D., Prochaska J. X., Bloom J. S., 2012, MNRAS, 426, 1465
Prieto J. L. et al., 2016, ApJ, 830, L32
Ramsden P., Lanning D., Nicholl M., McGee S. L., 2022, MNRAS, 515, 1146
Rayner J. T., Toomey D. W., Onaka P. M., Denault A. J., Stahlberger W. E., Vacca W. D., Cushing M. C., Wang S., 2003, PASP, 115, 362
Rees M. J., 1988, Nature, 333, 523
Reines A. E., Volonteri M., 2015, ApJ, 813, 82
Ricci C., Trakhtenbrot B., 2023, Nat. Astron., 7, 1282
Ricci C. et al., 2017, ApJS, 233, 17
Rich J. A., Kewley L. J., Dopita M. A., 2015, ApJS, 221, 28
Ricker G. R. et al., 2015, J. Astron. Telesc. Instrum. Syst., 1, 14003
Riess A. G. et al., 2022, ApJ, 934, L7
Rockosi C. et al., 2010, in McLean I. S., Ramsay S. K., Takami H.eds, Proc. SPIE Conf. Ser., Vol. 7735, Ground-based and Airborne Instrumentation for Astronomy III. SPIE, Bellingham. p. 77350R
Roming P. W. A. et al., 2005, SSR, 120, 95
Roth N., Kasen D., Guillochon J., Ramirez-Ruiz E., 2016, ApJ, 827, 3
Ryu T., Krolik J., Piran T., Noble S. C., 2020, ApJ, 904, 98
Sacchi A., Risaliti G., Miniutti G., 2023, A&A, 671, A33
Salpeter E. E., 1955, ApJ, 121, 161
Sarin N., Metzger B. D., 2024, ApJ, 961, L19
Saxton C. J., Perets H. B., Baskin A., 2018, MNRAS, 474, 3307
Sazonov S., Revnivtsev M., Krivonos R., Churazov E., Sunyaev R., 2007, A&A, 462, 57
Schlafly E. F., Finkbeiner D. P., 2011, ApJ, 737, 103
Sfaradi I., Horesh A., Bright J., Fender R., Rhodes L., Green D., Titterington D., 2023, Astron. Telegram, 15918, 1
Shappee B. J. et al., 2014, ApJ, 788, 48
Shiokawa H., Krolik J. H., Cheng R. M., Piran T., Noble S. C., 2015, ApJ, 804, 85
Short P. et al., 2020, MNRAS, 498, 4119
Short P. et al., 2023, MNRAS, 525, 1568
Skrutskie M. F. et al., 2006, AJ, 131, 1163
Smith J. A. et al., 2002, AJ, 123, 2121
Smith K. W. et al., 2020, PASP, 132, 085002
Springob C. M., Haynes M. P., Giovanelli R., Kent B. R., 2005, ApJS, 160, 149
Stanek K. Z., 2023, Transient Name Server Discovery Report, 2023-421, 1
Steinberg E., Stone N. C., 2022, Nature, 625, 463
Stern D. et al., 2004, ApJ, 612, 690
Stern D. et al., 2012, ApJ, 753, 30
Stone N. C., Kesden M., Cheng R. M., van Velzen S., 2019, Gen. Relativ. Gravit., 51, 30
Stritzinger M. D. et al., 2011, AJ, 142, 156
Strubbe L. E., Murray N., 2015, MNRAS, 454, 2321
Taguchi K., Uno K., Nagao T., Maeda K., 2023, Transient Name Server Classification Report, 2023-438, 1
Theureau G., Hanski M. O., Coudreau N., Hallet N., Martin J. M., 2007, A&A, 465, 71
Toba Y. et al., 2014, ApJ, 788, 45
Tonry J. L. et al., 2018a, PASP, 130, 64505
Tonry J. L. et al., 2018b, ApJ, 867, 105
Trakhtenbrot B. et al., 2019, ApJ, 883, 94

Tucker M. A. et al., 2021, MNRAS, 506, 6014
Tucker M. A. et al., 2022, PASP, 134, 124502
Tully R. B., Fisher J. R., 1977, A&A, 54, 661
Ulmer A., 1999, ApJ, 514, 180
Vallely P. J. et al., 2019, MNRAS, 487, 2372
Vallely P. J., Kochanek C. S., Stanek K. Z., Fausnaugh M., Shappee B. J., 2021, MNRAS, 500, 5639
Vanden Berk D. E. et al., 2001, AJ, 122, 549
van Velzen S., 2018, ApJ, 852, 72
van Velzen S. et al., 2011, ApJ, 741, 73
van Velzen S. et al., 2019a, ApJ, 872, 198
van Velzen S., Gezari S., Hung T., Gatkine P., Cenko S. B., Ho A., Kulkarni S. R., Mahabal A., 2019b, Astron. Tel., 12568, 1
van Velzen S., Holoien T. W. S., Onori F., Hung T., Arcavi I., 2020, Space Sci. Rev., 216, 124
van Velzen S. et al., 2021, ApJ, 908, 4
Veilleux S., Osterbrock D. E., 1987, ApJS, 63, 295
Vinkó J. et al., 2015, ApJ, 798, 12
Wang X.-Y., Liu R.-Y., 2016, Phys. Rev. D, 93, 83005
Wen S., Jonker P. G., Stone N. C., Zabludoff A. I., Psaltis D., 2020, ApJ, 897, 80
Wevers T. et al., 2019, MNRAS, 488, 4816
Woodgate B. E. et al., 1998, PASP, 110, 1183
Wright E. L. et al., 2010, AJ, 140, 1868
Yan R., Blanton M. R., 2012, ApJ, 747, 61
Yao Y. et al., 2023, ApJ, 955, L6
York D. G. et al., 2000, AJ, 120, 1579
Zabludoff A. et al., 2021, Space Sci. Rev., 217, 54
Zhang X.-G., 2021, MNRAS, 500, L57
Zhu J., Jiang N., Wang T., Huang S., Lin Z., Wang Y., Wang J.-G., 2023, ApJ, 952, L35

SUPPORTING INFORMATION

Supplementary data are available at *MNRAS* online.

Please note: Oxford University Press is not responsible for the content or functionality of any supporting materials supplied by the authors. Any queries (other than missing material) should be directed to the corresponding author for the article.

[1]*Institute for Astronomy, University of Hawaii, 2680 Woodlawn Drive, Honolulu, HI 96822, USA*
[2]*School of Physics, The University of Melbourne, Parkville, VIC 3010, Australia*
[3]*Department of Astronomy and Astrophysics, University of California, Santa Cruz, CA 95064, USA*
[4]*Department of Astronomy, The Ohio State University, 140 West 18th Avenue, Columbus, OH 43210, USA*
[5]*Center for Cosmology and AstroParticle Physics, The Ohio State University, 191 W. Woodruff Ave., Columbus, OH 43210, USA*
[6]*NASA Marshall Space Flight Center, Huntsville, AL 35812, USA*
[7]*Department of Physics, The Ohio State University, 191 West Woodruff Ave, Columbus, OH, USA*
[8]*Carnegie Observatories, Las Campanas Observatory, Casilla 601, La Serena 1700000, Chile*
[9]*The Observatories of the Carnegie Institution for Science, 813 Santa Barbara St., Pasadena, CA 91101, USA*
[10]*Núcleo de Astronomía de la Facultad de Ingeniería y Ciencias, Universidad Diego Portales, Av. Ejército 441, Santiago, Chile*
[11]*Millennium Institute of Astrophysics, Santiago, Chile*
[12]*Department of Physics and Astronomy, Aarhus University, Ny Munkegade 120, DK-8000 Aarhus C, Denmark*
[13]*TAPIR, Walter Burke Institute for Theoretical Physics, 350-17, Caltech, Pasadena, CA 91125, USA*
[14]*4Department of Physics and Astronomy, Purdue University, 525 Northwestern Avenue, West Lafayette, IN 47907, USA*
[15]*Department of Physics, Virginia Tech, Blacksburg, VA 24061, USA*
[16]*George P. and Cynthia Woods Mitchell Institute for Fundamental Physics and Astronomy, College Station, Texas 77843*
[17]*Department of Physics and Astronomy, Texas A&M University, College Station, TX 77843, USA*
[18]*Institute of Space Sciences (ICE-CSIC), Campus UAB, Carrer de Can Magrans, s/n, E-08193 Barcelona, Spain*
[19]*Institut d'Estudis Espacials de Catalunya (IEEC), E-08034 Barcelona, Spain*
[20]*Institute of Space Sciences (ICE-CSIC), Campus UAB, Carrer de Can Magrans, s/n, E-08193 Barcelona, Spain*
[21]*Institut d'Estudis Espacials de Catalunya (IEEC), E-08034 Barcelona, Spain*
[22]*Department of Physics, Florida State University, 77 Chieftan Way, Tallahassee, FL 32306, USA*
[23]*Department of Astronomy, University of Virginia, 530 McCormick Rd, Charlottesville, VA 22904, USA*
[24]*Department of Physics and Astronomy, Michigan State University, East Lansing, MI 48824, USA*

This paper has been typeset from a TEX/LATEX file prepared by the author.